

# An X-ray selected catalog of extended galaxy clusters from the ROSAT All-Sky Survey (RXGCC)

Weiwei Xu<sup>1,2</sup>, Miriam E. Ramos-Ceja<sup>3</sup>, Florian Pacaud<sup>2</sup>, Thomas H. Reiprich<sup>2</sup>, and Thomas Erben<sup>2</sup>

<sup>1</sup> The Kavli Institute for Astronomy and Astrophysics at Peking University (KIAA-PKU), Peking University, Yiheyuan Road 5, 100871 Beijing, China (e-mail: [wwxu@pku.edu.cn](mailto:wwxu@pku.edu.cn))

<sup>2</sup> Argelander-Institut für Astronomie (AIfA), Universität Bonn, Auf dem Hügel 71, 53121 Bonn, Germany

<sup>3</sup> Max-Planck-Institut für extraterrestrische Physik, Giessenbachstraße, 85748 Garching, Germany

Received xx, 202x; accepted xx, 202x

## ABSTRACT

**Context.** There is a known tension between cosmological parameter constraints obtained from the primary cosmic microwave background (CMB) and those from galaxy cluster samples. One possible explanation for this discrepancy could be that the incompleteness of detected clusters is higher than estimated, and certain types of groups or clusters of galaxy have been missed in the past.

**Aims.** We aim to search for galaxy groups and clusters with particularly extended surface brightness distributions, by creating a new X-ray selected catalog of extended galaxy clusters from the ROSAT All-Sky Survey (RASS), using a dedicated source detection and characterization algorithm optimized for extended sources.

**Methods.** Our state-of-the-art algorithm includes multi-resolution filtering, source detection and characterization. Through extensive simulations, the detection efficiency and sample purity are investigated. Previous cluster catalogs in X-ray and other wave-bands, as well as spectroscopic and photometric redshifts of galaxies are used for the cluster identification.

**Results.** We report a catalog of galaxy clusters at high galactic latitude based on the ROSAT All-sky Survey, named as RASS-based extended X-ray Galaxy Cluster Catalog (RXGCC), which includes 944 groups and clusters. Out of this number, 641 clusters have been identified through intra-cluster medium (ICM) emission previously (*Bronze*), 154 known optical and infrared clusters are detected as X-ray clusters for the first time (*Silver*), and 149 identified as clusters for the first time (*Gold*). Based on 200 simulations, the contamination ratio of the detections which were identified as clusters by ICM emission, and the detections which were identified as optical and infrared clusters in previous work is 0.008 and 0.100, respectively. Compared with *Bronze* sample, the *Gold + Silver* sample is less luminous, less massive, and has a flatter surface brightness profile. Specifically, the median flux in [0.1 – 2.4] keV band for *Gold + Silver* and *Bronze* sample is  $2.496 \times 10^{-12}$  erg/s/cm<sup>2</sup> and  $4.955 \times 10^{-12}$  erg/s/cm<sup>2</sup>, respectively. The median value of  $\beta$  (the slope of cluster surface brightness profile) is 0.76 and 0.83 for *Gold + Silver* and *Bronze* sample, respectively. This whole sample is available at [https://github.com/wwxu/rxgcc.github.io/blob/master/table\\_rxgcc.fits](https://github.com/wwxu/rxgcc.github.io/blob/master/table_rxgcc.fits).

**Conclusions.**

**Key words.** X-rays: general catalogs-surveys-galaxy cluster

## 1. Introduction

Among the different cosmological probes, galaxy clusters are one of the most important ones to test the standard cosmological scenarios (Dunkley et al. 2009; Kowalski et al. 2008; Reiprich & Böhringer 2002; Seljak 2002; Dahle 2006; Pedersen & Dahle 2007; Rines et al. 2007; Wen et al. 2010; Allen et al. 2008, 2011; Abbott et al. 2018). As the largest gravitational systems in the universe, their spatial distribution and number density are sensitive to the dark matter and dark energy content (e.g., Borgani et al. 2001; Reiprich & Böhringer 2002; Seljak 2002; Viana et al. 2002; Kravtsov & Borgani 2012; Schellenberger & Reiprich 2017). However, cosmological constraints derived from the primary cosmic microwave background (CMB, Planck Collaboration et al. 2016, 2020a,b; Abbott et al. 2020) and those from galaxy cluster studies are in tension (see, e.g., Fig. 17 in Pratt et al. 2019). One of the possible explanations is the underestimation of the incompleteness of detected clusters.

The intra-cluster medium (ICM) allows us to detect galaxy clusters using two different wavelengths: X-ray and sub-millimetre bands. Compared with cluster observation in other bands, such as in optical wavelength, the ICM observation trace genuine deep gravitational potential wells, and is less affected by projection effects. The X-ray emission includes the bremsstrahlung and line emission (e.g., Reiprich et al. 2013), while sub-millimeter emission comes from the Sunyaev-Zel'dovich effect (Sunyaev & Zeldovich 1970, 1972, 1980).

Kinds of methods are used to detect galaxy clusters in X-ray data. The most widely used are the sliding-cell algorithm (e.g. Voges et al. 1999), the Voronoi tessellation and percolation method (VTP, Ebeling & Wiedenmann 1993; Scharf et al. 1997; Perlman et al. 2002), and the wavelet transformation (Rosati et al. 1995; Vikhlinin et al. 1998; Pacaud et al. 2006; Mullis et al. 2003; Lloyd-Davies et al. 2011; Xu et al. 2018). These methods have distinct

advantages and disadvantages of cluster detections (e.g. Valtchanov et al. 2001).

Up to the mid-2019, ROSAT was the only X-ray telescope performed an all-sky imaging survey (RASS, Truemper 1992, 1993) in the 0.1 – 2.4 keV energy band. There are several ROSAT-based cluster catalogs, some of the most important are: REFLEX (ROSAT-ESO Flux Limited X-ray Galaxy Cluster Survey, Böhringer et al. 2004), NORAS (Northern ROSAT All-Sky galaxy cluster survey, Böhringer et al. 2000, 2017), BCS (ROSAT Brightest Cluster Sample, Ebeling et al. 1998, 2000), SGP (a Catalog of Clusters of Galaxies in a Region of 1 steradian around the South Galactic Pole, Cruddace et al. 2002), NEP (the ROSAT North Ecliptic Pole survey, Henry et al. 2006), and MACS (Massive Cluster Survey, Ebeling et al. 2001). These catalogues, and few more, have been compiled in the so-called MCXC catalogue (Meta-Catalogue of X-ray detected Clusters, Piffaretti et al. 2011). Besides ROSAT, XMM-Newton and Chandra observatories are also widely used to identify galaxy clusters. With better resolution and sensitivity, and longer exposure times, they could identify faint clusters at high redshift, such as the works of Mehrrens et al. (2012), Clerc et al. (2012), Clerc et al. (2016), Takeya et al. (2011, 2013, 2014, 2016), Pacaud et al. (2016), to list a few.

As the successor of ROSAT, the eROSITA X-ray satellite (extended Roentgen Survey with an Imaging Telescope Array, Merloni et al. 2012) is scanning the whole sky in the 0.1 – 10 keV energy band. eROSITA will complete 8 scannings in its first 4 years, and reach a sensitivity of 25 times better<sup>1</sup> than ROSAT (Predehl et al. 2020). It will be able to make a complete detection of clusters with  $M > 2 \times 10^{14} M_{\odot}$ , detect  $> 100,000$  galaxy clusters, and thus allow us to set tighter constraints on dark energy (e.g., Merloni et al. 2012, 2020; Pillepich et al. 2012, 2018). First results indeed look very promising (e.g., Ghirardini et al. 2021; Reiprich et al. 2021). However, it will take time until the first full sky eROSITA cluster catalogs are published.

In Xu et al. (2018) (hereafter Paper I), we applied an X-ray, wavelet-based, source detection algorithm to the RASS data, and found many known as well as many new candidates of galaxy groups and clusters, which were not included in any previous X-ray or SZ (detected by the Sunyaev-Zel'dovich effect in micro-wave band) cluster catalogues. Out of those, we showed a pilot sample of 13 very extended groups, whose surface brightness distributions are flatter than expected and, some of them have X-ray fluxes above the nominal flux-limits of previous RASS cluster catalogues. We argued that such galaxy groups were missed in previous RASS surveys due to their flat surface brightness distribution, which was not detected by the sliding-cell algorithm.

In this paper, we release our final galaxy cluster catalogue, the RASS-based X-ray selected extended Galaxy Clusters Catalog (RXGCC), and discuss the cluster properties (e.g., position and redshift, angular size, X-ray luminosity, mass, etc.). The paper is structured as follows. Section 2 describes the data and methodology briefly. Section 3 presents the RXGCC catalog, and the distribution of parameters. In Section 4, we discuss the very extended

clusters and false detections in our work, and compare the RXGCC catalog with other ICM-detected cluster catalogs and a general X-ray source catalog. Section 5 shows the conclusion of this project.

Additional information is added in the appendix. We discuss the difference between the method applied here and that of Paper I in Sec. A. In Sec. B, we estimate the contamination ratio for detections with simulations. In Sec. C, we show the comparison of detected and undetected MCXC, PSZ2, Abell clusters. In Sec. D, we compare detected and undetected REFLEX and NORAS clusters. In Sec. E, we show the gallery of two clusters as example. In Sec. F, we list clusters whose redshift or classification is changed using the visual check.

Throughout the paper, we assume the cosmological parameters as  $H_0 = 70 \text{ km s}^{-1} \text{ Mpc}^{-1}$ ,  $\Omega_M = 0.3$ , and  $\Omega_{\Lambda} = 0.7$ .

## 2. Data and methodology

In this section, we present a brief description of the data and the methodology to detect, classify, and characterize sources. Further details are provided in Paper I, and method modifications are discussed in Sec. A.

### 2.1. Data

We use the RASS images in the 0.5 – 2.0 keV energy band. These images come from the third processing of the RASS data (RASS-3<sup>2</sup>). We exclude the regions within galactic latitude  $|b| < 20^\circ$ , the Virgo cluster, the Large and Small Magellanic Clouds (see Tab. 2 in Reiprich & Böhringer 2002). The total data coverage in this work is 26,721.8 deg<sup>2</sup> (8.13994 sr), about two-thirds of the sky.

### 2.2. Source detection

Our source detection and characterization method consists of three main steps. First, we apply a multi-resolution wavelet filtering procedure (Pacaud et al. 2006; Faccioli et al. 2018) to remove the Poisson noise in the RASS images. Secondly, we use the SExtractor software (Bertin & Arnouts 1996) on the filtered images. Finally, a maximum-likelihood fitting algorithm models each detected source. This last step makes use of C-statistics (Cash 1979) and fits two models to each source: a point source model, given by the point-spread function (PSF) of the PSPC detector, and a cluster model, described by a  $\beta$ -model with  $\beta = 2/3$  (Cavaliere & Fusco-Femiano 1976). The  $\beta$ -model describes the surface-brightness of galaxy clusters with a spherically symmetric model,  $S_x(r) \propto [1 + (r/r_c)^2]^{-3\beta+0.5}$ , where  $r_c$  is the core radius of the cluster, and  $\beta$  describes the slope of the brightness profile. The value of  $\beta$  is 2/3 for a typical cluster. The smaller  $\beta$ , the flatter the profile.

The maximum-likelihood fitting algorithm outputs several parameters for each source. Using extensive Monte Carlo simulations (see Paper I for further details), we calibrate and find criteria to classify the detections. The simulations include a realistic sky and particle background, a population of AGN, and galaxy clusters with different

<sup>1</sup> It refers to the flux limit for point sources, which is  $5 \times 10^{-13} \text{ erg/s/cm}^2$  and  $1.1 \times 10^{-14} \text{ erg/s/cm}^2$  for RASS (0.5 – 2.0 keV) and eRASS-8 (0.2 – 2.3 keV, Predehl et al. 2020).

<sup>2</sup> [https://heasarc.gsfc.nasa.gov/FTP/rosat/data/pSPC/processed\\_data/rass/release/](https://heasarc.gsfc.nasa.gov/FTP/rosat/data/pSPC/processed_data/rass/release/)

profile, size, and flux. We have chosen the *detection likelihood* (i.e. the significance of each detection compared with a background distribution), the *extension likelihood* (i.e. the significance of the source extension), and the *extent* (i.e. the core radius of the cluster model), as best parameters to classify our detections. It is expected the false detection rate is  $0.0024/\text{deg}^2$  with the thresholds of *detection likelihood*  $> 20$ , *extension likelihood*  $> 25$  and *extent*  $> 0.67$  arcmin.

### 2.3. Classification of detections

To classify the detections, we consider not only the spatial and redshift distribution of galaxies, but also the information from previously identified clusters. As described in this subsection, we collect galaxy redshifts and identify clusters, to estimate the redshift and classify our detections based on the classification criteria. In the last step, we visually inspect images in multiple bands to confirm our redshift estimation and classification.

#### 2.3.1. Redshift estimation

To estimate redshifts of the detections, we gather all spectroscopic and photometric redshifts of galaxies located within 15 arcmin surrounding our detections, with  $0 < z < 0.4$ , from the Sloan Digital Sky Survey (SDSS) DR16<sup>3</sup>, Galaxy And Mass Assembly DR1<sup>4</sup> (GAMA), the Two Micron All Sky Survey Photometric Redshift Catalog (2MPZ catalog, Bilicki et al. 2014) and the NASA Extragalactic Database<sup>5</sup> (NED). We consider galaxies as the same object if the offset  $< 3''$  and  $\Delta z < 0.01$ , and only reserve the information of one galaxy in the following priority order: SDSS, GAMA, 2MPZ, NED. The spectroscopic redshift in surveys has a higher priority than the photometric redshift.

This way, we obtain the distribution of galaxy redshifts, both spectroscopic and photometric ones, for each detection. The galaxy redshifts are binned with the width of  $\Delta z = 0.01$ . We iteratively fit a Gaussian function with  $3\sigma$  clipping to the two highest peaks in the distribution. Each peak should contain  $\geq 3$  redshifts. The best fit value is taken as the candidate redshift. Note that the second peak is also taken as an alternative option of the candidate redshift, in case of the included galaxy number is no less than 20% of the highest peak. The redshift difference of the two candidate values is set as  $\Delta z > 0.02$  to avoid the overlap. Furthermore, the  $1\sigma$  redshift dispersion is estimated, including the intrinsic cluster velocity dispersion and the uncertainty of redshift estimation. The redshift error is set as  $\sigma_z > 0.005$ .

In addition, we perform a visual inspection (see Sec. 2.3.4) to confirm the redshift of detections. If there are not enough galaxy redshifts measured, the final redshift is obtained from the collected redshift information of known galaxy clusters, if available. ICM-detected cluster information has a higher priority than optical cluster information. All this information, if applicable, is added to the 'z,src' column of Tab. 3.

<sup>3</sup> <http://www.sdss.org>

<sup>4</sup> <http://www.gama-survey.org>

<sup>5</sup> <https://ned.ipac.caltech.edu>

#### 2.3.2. Collection of identified clusters

We perform an extensive cross-matching of our detections with other publicly available cluster catalogues to determine how many detections have been identified as clusters or groups previously. We collect the information of galaxy clusters from the literature, and list them in Tab. 1. As mentioned in Sec. 1, the MCXC catalog is a meta-catalog that includes a number of individual catalogs, such as the REFLEX and NORAS catalogs. In addition, we take into account systems from the NED database, which are classified as *cluster of galaxies*, *group of galaxies*, *galaxy pair*, *galaxy triple*, or *group of QSOs*. We discard these NED systems with the name beginning with *WHL*, *MCXC* or *PSZ2*, to avoid the repetition with catalogs from the literature.

Given that the Abell and ICM-detected clusters have a limited accurate redshift, we also cross-match detections with them only by projected distance without considering their redshifts, and list the cross-matching result in the last column of Tab. 3 as a reference. This information is not used to classify our detections, which is discussion in Sec. 2.3.3.

Besides the cluster catalogs, we also list ROSAT X-ray point-source catalogs in the last part of Tab. 1, see Sec. 4.4 for details.

#### 2.3.3. Classification Criteria

We cross-match our detections with previously identified clusters described in Sec. 2.3.2, using a matching radius of  $15'$  and  $0.5$  Mpc, and  $\Delta z < 0.01$ . If all criteria are met for two clusters, we consider them as the same one. With these criteria and visual inspection, we classify our detections into four classes:

- *Gold*, if the detection is not cross-identified with any known optical, infrared, X-ray or SZ cluster, and performs as a clear galaxy over-density in optical and infrared images and/or has a clear peak in the distribution of galaxy redshifts.
- *Silver*, if the detection has been cross-identified with a known optical or infrared cluster, but not cross-identified with any X-ray or SZ cluster.
- *Bronze*, if the detection has been cross-identified with known X-ray or SZ cluster.
- *False detections*, if the detection seems a spurious detection, or if it is artificially created by multiple high-redshift clusters that are nearby located in projection.

#### 2.3.4. Visual inspection

We create an extensive multi-wavelength gallery for each of our detections. For each source, we checked the RASS photon image, RASS exposure map, wavelet-reconstructed image, as well as the galactic neutral hydrogen column density image from the HI4PI survey (HI4PI Collaboration et al. 2016). These images, combined with galaxy redshifts described in Sec. 2.3.1, help us to find out detections artificially created by the large variation of exposure time, or a low hydrogen column density along the line-of-sight. Furthermore, when available, we inspected image from the *Planck*<sup>6</sup> survey (refer Erler et al. 2018 for the corresponding image extraction method), infrared RGB image from

<sup>6</sup> <http://www.esa.int/Planck>

Table 1: Overview of cluster catalogs and X-ray point-source catalogs.

Catalogs	Reference	$N_{gc}$	$N_{gc}(\text{with } z)$	Survey	
X-ray catalogs	Finoguenov et al. 2020	10 382	10 382	ROSAT	
	Takey et al. 2011, 2013, 2014, 2016	904	904	<i>XMM-Newton</i> , SDSS	
	Clerc et al. 2020; Kirkpatrick et al. 2021	2 740	2 740	ROSAT	
	Clerc et al. 2016	240	240	ROSAT, <i>XMM-Newton</i>	
	Clerc et al. 2012	422	176*	<i>XMM-Newton</i> XXL	
	Pacaud et al. 2016	100	100	<i>XMM-Newton</i> XXL	
	Liu et al. 2015	263	0	Swift	
	Mehrtens et al. 2012	503	463	<i>XMM-Newton</i>	
	Piffaretti et al. 2011	1 743	1 743	ROSAT	
	Ledlow et al. 2003	579	579	ROSAT	
	Ebeling et al. 1996	283	278	ROSAT	
	Microwave catalogs	Tarrío et al. 2019	2 323	1 459	<i>Planck</i> , RASS
		Tarrío et al. 2018	225	171	<i>Planck</i> , RASS
		Hilton et al. 2018	182	182	ACT
Planck Collaboration et al. 2016		1 653	1 094	<i>Planck</i>	
Bleem et al. 2015		677	649	SPT	
Hasselfield et al. 2013		91	91	ACT	
Marriage et al. 2011		23	23	ACT	
Optical & Infrared catalogs	Oguri et al. 2018	1 921	1 921	HSC	
	Oguri 2014	71 743	71 743	SDSS	
	Rykoff et al. 2016	26 898	26 898	SDSS	
	Rykoff et al. 2014	25 325	25 325	SDSS	
	Wen et al. 2018	47 600	47 600	2MASS, WISE, SuperCOSMOS	
	Wen & Han 2015	25 419	25 419	SDSS	
	Wen et al. 2012	132 684	132 684	SDSS	
	Abell 1958; Abell et al. 1989	5524	875	-	
	X-ray point-source catalogs	Voges et al. 1999			ROSAT
Voges et al. 2000				ROSAT	
Boller et al. 2016				ROSAT	

\* For the reliability, we take into account clusters with redshift status as "confirmed" (spectroscopic) or "photometric", and discard those with redshift status as "provisional" or "tentative".

2MASS<sup>7</sup>, optical image from the POSS2/UKSTU Red survey<sup>8</sup>, and optical RGB image (combination of  $i$ ,  $r$  and  $g$  bands) from VST ATLAS<sup>9</sup>, Pan-STARRS1<sup>10</sup>, DES DR1<sup>11</sup>, and SDSS DR12.

The detections of M101 (RA: 210.828°, DEC: 54.313°) and M51 (RA: 202.495°, DEC: 47.211°) are confirmed as galaxies using the visual inspection, thus removed from the final catalog.

In addition, visual inspection is performed to confirm, and modify if needed, the redshift and classification of detections. The modifications are listed in Tab. F.1.

- Whether the spatial distribution of member galaxies obeys the cluster morphology, (*yes* for the existence of a cluster),
- Whether a bright elliptical galaxy is found at the central region, (*yes* for the existence of cluster),
- Whether the X-ray emission mainly comes from a star, star cluster, galaxy, or AGN, (*yes* for false detection).

#### 2.4. Characteristics of cluster candidates

After the source detection and classification, we estimate physical parameters, such as the size, flux, luminosity, and mass, to characterize cluster candidates. Besides that, we also estimate their  $\beta$ -value to show the compactness.

<sup>7</sup> <https://www.ipac.caltech.edu/2mass>

<sup>8</sup> <http://archive.eso.org/dss/dss>

<sup>9</sup> <http://astro.dur.ac.uk/Cosmology/vstatlas>

<sup>10</sup> <https://panstarrs.stsci.edu>

<sup>11</sup> <https://www.darkenergysurvey.org>

##### 2.4.1. Estimation of physical parameters

We estimate X-ray observables using the growth curve analysis method (Böhringer et al. 2000; Böhringer et al. 2001), which is briefly described in this subsection. Firstly, the growth curve, i.e. the cumulative count-rate of photons as a function of radius, is constructed for each cluster in the [0.5 – 2.0] keV energy band. The regions within the radius of 20', 40', and 60' are taken as the source area, respectively. In some complex cases, other radius is taken for the source area, such as 30', 50', or 80'. A larger annulus with the width of 20' is used to estimate the local background. Contamination in the background and source area, from projected foreground or background sources, is corrected using a de-blending procedure, which excludes angular sectors with count rate different from the median value by  $> 2.3\sigma$ .

After the background is subtracted, we bin the growth-curve with the width of 0.5'. The growth curve is supposed to be flat at large radius, where the contribution of cluster is negligible. We define the significant radius,  $R_{sig}$ , as the radius whose  $1\sigma$  uncertainty interval encompasses all count rates integrated in larger apertures. We take the growth curve beyond the significant radius as the plateau, and take the average plateau count rate as the significant count rate,  $CR_{sig}$ . For each candidate, the source aperture with the most steady growth curve is used for following analysis.

With the estimation of  $R_{sig}$  and  $CR_{sig}$ , we calculate the main parameters with the scaling relations from Reichert et al. (2011), the Eq. 23-26 wherein show the power-law relations between  $L_x$ ,  $T_x$ , and  $M$ . Firstly, we assume  $R_{500} = R_{sig}$ , and obtain the total mass within  $R_{500}$  ( $M_{500}$ ), and further the bolometric X-ray luminosity ( $L_x$ ) and temperature ( $T_x$ ), using scaling relations. With the APEC model,

we obtain the luminosity within  $R_{500}$  in  $[0.1 - 2.4]$  keV band ( $L_{500}$ ), as well as the flux in the same band ( $F_{500}$ ). The total count rate inside  $R_{500}$  ( $CR_{500}$ ) is further estimated with PIMMS (Mukai 1993), taking into account the instrument response of ROSAT PSPC, and the galactic absorption. Using the typical  $\beta$ -profile with  $\beta = 2/3$ , we take the value of  $CR_{500}$  as an estimation of  $CR_{\text{sig}}$ . The goal is that the estimated  $CR_{\text{sig,est}}$  is equal to the observed  $CR_{\text{sig,obs}}$ . Therefore, the steps described above are iteratively repeated until  $CR_{\text{sig,est}} = CR_{\text{sig,obs}}$ . This way, we obtain the value of  $CR_{500}$  and  $R_{500}$ , as well as corresponding parameters, such as  $M_{500}$ ,  $L_{500}$ ,  $T_x$ , and  $F_{500}$ .

#### 2.4.2. Estimation of $\beta$ value

To better understand the clusters in our sample, we characterise their X-ray emission profile. As mentioned in Sec. 2.2, the  $\beta$  value describes the flattening of the source. And the  $\beta$  parameter is highly correlated with the core radius.

Using the Markov Chain Monte Carlo (MCMC) method, we estimate the value and uncertainty of the  $\beta$  and the core radius, by fitting the growth curve with a  $\beta$ -model convolved with the PSF. For the simplicity, we take a gaussian function with the FWHM of 45 arcsec as the PSF of the PSPC detector. In the MCMC fitting<sup>12</sup>, we use 50 chains in total, 10000 steps each. The free parameters include the  $\beta$  value, the core radius, and the normalization. We initialize chains in a tiny range around the maximum likelihood result, and discard first 5000 steps of each chain to avoid the effect from the starting point. Then, a uniform prior is assumed for each parameter, whose threshold is set as respectively 0.50 and 1.00 for  $\beta$  value, 0.01 and 50.0 arcmin for the core radius, 0.001 and 5 for the normalization. The lower limit of the  $\beta$  value comes from the convergence requirement of the integrated count rate.

### 3. Results

We obtain 1308 detections with the RASS data in the high galactic latitude area. Following the source detection, classification and characterization methods described in Sec. 2, we obtain 641 *Bronze* clusters, 154 *Silver* clusters, and 149 *Gold* clusters. These 944 cluster candidates are compiled into the final catalog, named as the RASS-based X-ray selected Galaxy Cluster Catalog (RXGCC). A detailed discussion about false detections is provided in Sec. 4.2. The distribution of each class in the *extent - extension likelihood* parameter space (see Sec. 2.2) are shown in Fig. 1, and the source number and median redshift are summarized in Tab. 2.

Table 2: The detections in classes.

Class	Number	Median redshift
<i>Gold</i>	149	0.0914
<i>Silver</i>	154	0.0584
<i>Bronze</i>	641	0.0780
<i>False detections</i>	364	-

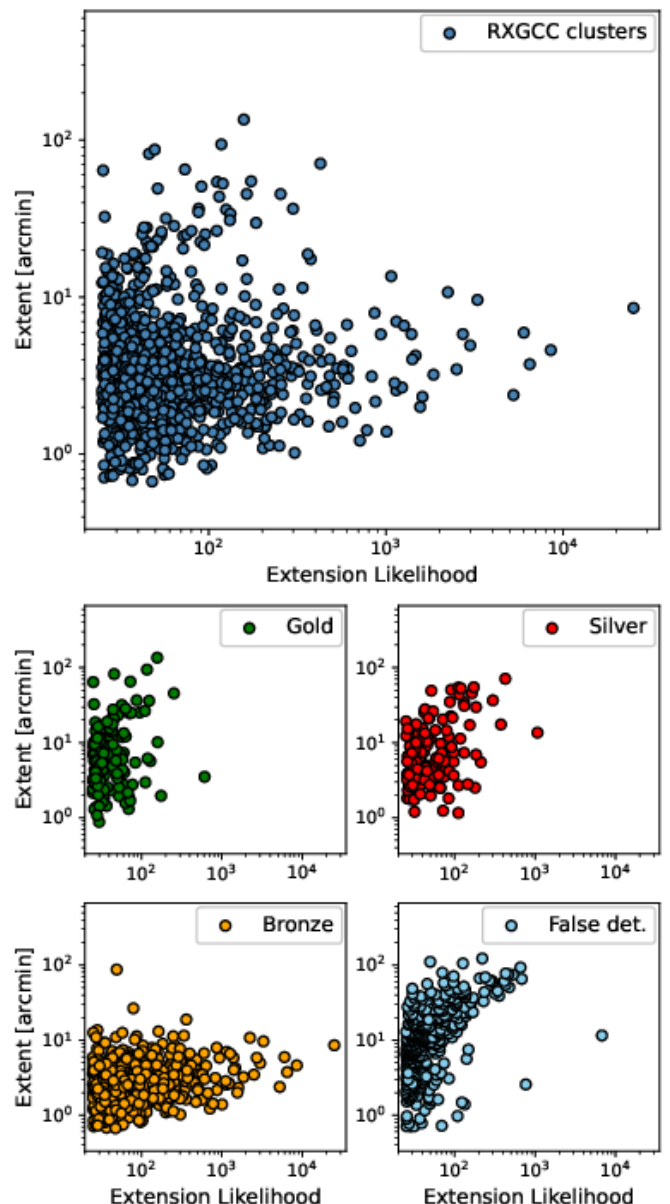


Fig. 1: *Extent - extension likelihood* plane that defined our criteria to select extended X-ray sources (see Paper I for further details). In the top panel, we show the RXGCC clusters, i.e., *Gold+Silver+Bronze*. The following top-left, top-right, and bottom-left panels show sub-samples of RXGCC: *Gold* - new identified clusters, *Silver* - previous optical/infrared-identified clusters, *Bronze* - previous ICM-identified clusters. The bottom-right panel shows the *False detection* - spurious detections.

The redshift distribution of RXGCC clusters is shown in Fig. 2. It shows that the newly-identified clusters (*Gold*) tend to have a little higher redshift than the clusters previously identified as optical/infrared clusters (*Silver*), while the previously ICM-identified clusters (*Bronze*) have a consistent redshift distribution with the whole RXGCC sample, whose median redshift is 0.0770. The redshift histogram demonstrates the detection efficiency decreases greatly when the redshift  $z > 0.12$ .

The highest redshift of the sample is 0.5551, and there are four RXGCC clusters with  $z > 0.4$  (RXGCC 229, RXGCC 237, RXGCC 306, RXGCC 590). These redshifts

<sup>12</sup> EMCEE package: <https://emcee.readthedocs.io/en/stable/>

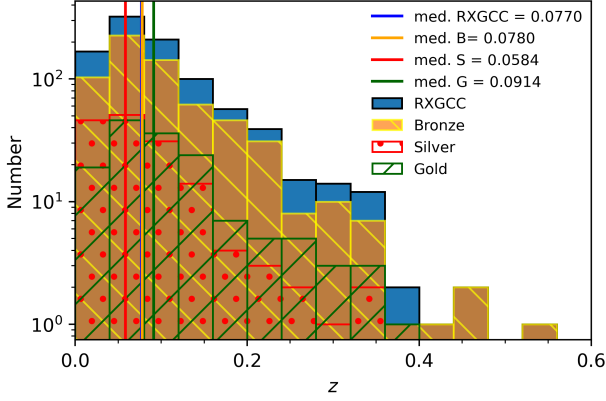


Fig. 2: Redshift distribution for different classes of our cluster candidates. The overlaid vertical line indicates the median redshift of different classes. For the simplicity, we use 'G', 'S', and 'B' for short of the *Gold*, *Silver*, and *Bronze* sample.

are obtained from previous ICM-detected clusters, instead of galaxy redshifts. A careful visual check of X-ray and micro-wave images, the spatial distribution and distance between these four detections and previous-identified clusters, makes the evidence strong enough to say the detected X-ray emission indeed comes from the previously-identified clusters. For these four candidates, the redshift limit of cross-matched clusters is set as  $z < 0.6$ , instead of  $z < 0.4$ , and the offset threshold is  $< 1.5$  Mpc, instead of  $< 0.5$  Mpc.

In addition, three clusters, RXGCC 406, RXGCC 639, and RXGCC 646, are covered with deep optical observation. In the redshift estimation, galaxy redshifts are constrained as  $< 0.16$ , instead of  $< 0.4$ .

For the cross-matching of RXGCC with previous ICM-detected clusters, there are several exceptions. RXGCC 93, RXGCC 239, RXGCC 612, RXGCC 688 have ICM-identified clusters in  $< 15'$ , but the position and redshift distribution of galaxies indicate clearly that the previous ICM-detect clusters are not what we detected. Thus, we remove them out of *Bronze* and classify them as *Gold* or *Silver* further.

### 3.1. RXGCC catalog

The RXGCC catalog comprises 944 clusters, including 641 *Bronze*, 154 *Silver*, and 149 *Gold* clusters, whose spatial distribution is shown in the top panel of Fig. 3. The full table is sorted with Right Ascension and is provided in FITS format as supplement material ([https://github.com/wwxu/rxgcc.github.io/blob/master/table\\_rxgcc.fits](https://github.com/wwxu/rxgcc.github.io/blob/master/table_rxgcc.fits)). The first 10 rows of the RXGCC catalog are shown in Tab. 3 and Tab. 4 for its form and content. In addition, we also publish the image gallery for each RXGCC source. For example, the gallery for RXGCC. 1 is shown in the following page, <https://github.com/wwxu/rxgcc.github.io/blob/master/script/1.md>.

In Tab. 3, the first five columns are the name, position, *extent* and *extension likelihood* values. The RXGCC cluster coordinates are obtained from the maximum-likelihood fitting (see Sec. 2.2). The 6th and 7th columns are the estimation of redshift and its error (see Sec. 2.3.1). The 8th column shows the source of the cluster redshift, referring the

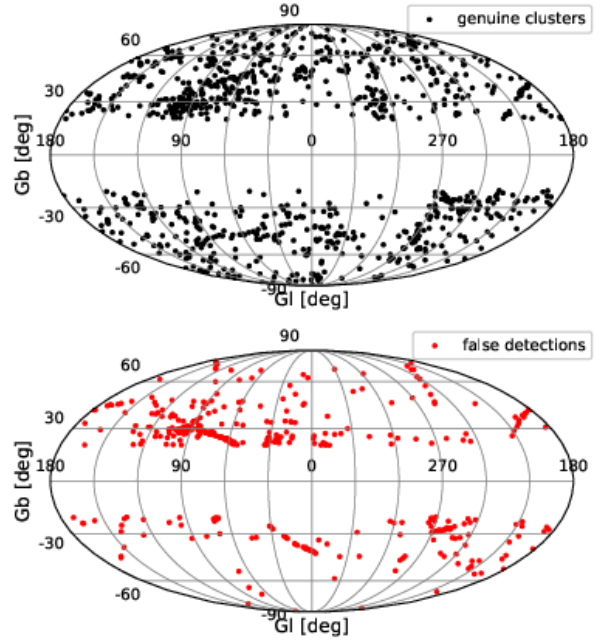


Fig. 3: *Top*: The all-sky distribution of RXGCC clusters. *Bottom*: The all-sky distribution of false detections.

table note for the detail. The 9th column shows the classification, described in Sec. 2.3.3. The following two columns contain information on the cross-matching with previously ICM-identified clusters, and clusters previously identified in optical or infrared band. These clusters are all offset from our candidates  $< 0.5$  Mpc and  $< 15'$ , and the redshift difference  $\Delta z < 0.01$ . The last column lists the Abell clusters or ICM-detected clusters within 0.5 Mpc and  $15'$ , regardless of their redshift value.

Table 3: The first part of the first 10 entries in the RXGCC catalog.

RXGCC	RA J2000 [°] (2)	Dec J2000 [°] (3)	Extent [arcmin] (4)	Ext,ml (5)	z (6)	z,err (7)	z,src** (8)	C† (9)	GC(XSZ,Δz < 0.01)† (10)	GC(OPT,Δz < 0.01)- (11)	GC* (12)
1	0.026	8.279	2.13	56.61	0.0364	0.005	z1, z-xsz	B	MCXC	N	C, F20, MCXC, N, SPI, W
2	0.641	8.451	6.41	42.14	0.0961	0.005	z1, z-xsz	B	F20, SPI	A, W	A, C, F20, N, SPI, W
3	0.797	-35.946	3.04	128.14	0.0493	0.005	z1, z-xsz	B	MCXC, Tar, XB	A, N	A, MCXC, N, Tar, W, XB
4	1.339	16.223	3.36	85.08	0.1154	0.005	z1, z-xsz	B	F20, MCXC	C, N, RM, W	A, C, F20, MCXC, N, W
5	1.497	-34.702	2.12	55.62	0.1145	0.005	z1, z-xsz	B	MCXC, PSZ2, Tar, XB	A, W	A, MCXC, N, PSZ2, Tar, W, XB
6	1.585	10.866	1.73	28.41	0.1666	0.005	z1, z-xsz	B	F20, MCXC, PSZ2, SPI, Tar	C, N, RM, W, Zw	C, F20, MCXC, N, PSZ2, SPI, Tar, W
7	2.556	2.093	8.87	25.46	0.1577	0.005	z1,	G	-	-	C, N, W
8	2.700	-81.160	6.66	26.49	0.1246	0.005	z1, z-opt	S	W	W	W
9	2.823	-28.848	2.07	136.69	0.0616	0.005	z1, z-xsz	B	MCXC, PSZ2, Tar, XB	A, W	A, MCXC, N, PSZ2, Tar, W, XB
10	2.935	32.415	1.32	61.24	0.1036	0.005	z1, z-xsz	B	F20, MCXC, PSZ2, SPI, Tar, XB	A, C, RM, W	A, C, F20, MCXC, PSZ2, SPI, Tar, W, XB

† For the simplicity, we use 'G', 'S', and 'B' for short of the *Gold*, *Silver*, and *Bronze* class.

\*\* The source of the redshift. 'z1' means the redshift comes from the highest peak of the redshift histogram of galaxies, while 'z2' for the second highest peak. 'z-opt' and 'z-xsz' shows the redshift of candidate matches with or comes from (when no 'z1' nor 'z2' available) the previous identified optical clusters or ICM-detected clusters.

+ Previously ICM-identified clusters within 0.5 Mpc, 15' and Δz < 0.01: F20 (Finoguenov et al. 2020), Tak (Takey et al. 2011, 2013, 2014, 2016), SPI (Clerc et al. 2012, Clerc et al. 2016, Clerc et al. 2020, Kirkpatrick et al. 2021), XLSSC (Pacaud et al. 2016), SWXCS (Liu et al. 2015), XCS (Mehrtens et al. 2012), MCXC (Piffaretti et al. 2011), L03 (Ledlow et al. 2003), XB (XBACs, Ebeling et al. 1996), Tar (Tarrío et al. 2018, 2019), H18 (Hilton et al. 2018), PSZ2 (Planck Collaboration et al. 2016), B15 (Bleem et al. 2015), H13 (Hasselfield et al. 2013), M11 (Marriage et al. 2011).

- Clusters detected in optical or infrared band within 0.5 Mpc, 15' and Δz < 0.01: C (CAMIRA, Oguri 2014; Oguri et al. 2018), Zw (Zwicky & Kowal 1968), RM (redMaPPer, Rykoff et al. 2014, 2016), W (Wen et al. 2012; Wen & Han 2015; Wen et al. 2018), A (Abell 1958; Abell et al. 1989), N for clusters from NED database.

\* The Abell clusters and ICM-detected clusters within 0.5 Mpc and 15', regardless of their redshifts.

(This table is available in the online journal. The first ten entries are shown here for its form and content.)

Table 4: The second part of the first 10 entries of the RXGCC catalog.

RXGCC	Rsig [arcmin] (2)	R500 [arcmin] (3)	R500 [Mpc] (4)	CRsig [c/s] (5)	CR500 [c/s] (6)	L500† [10 <sup>44</sup> erg/s] (7)	F500† [10 <sup>-12</sup> erg/s/cm <sup>2</sup> ] (8)	M500† [10 <sup>14</sup> M <sub>⊙</sub> ] (9)	Tx† [keV] (10)	Cnt <sub>sig</sub> <sup>-</sup> (11)	β (12)
1	13.188	14.734	0.639	0.265 (0.037)	0.270 (0.038)	0.137 (0.013)	4.457 (0.410)	0.77 (0.04)	1.84 (0.05)	128	0.74
2	40.600	9.572	1.023	0.442 (0.071)	0.392 (0.063)	1.677 (0.462)	7.202 (1.982)	3.33 (0.45)	4.64 (0.40)	303*	0.50
3	31.612	14.921	0.864	0.735 (0.084)	0.676 (0.077)	0.772 (0.067)	13.443 (1.158)	1.92 (0.08)	3.25 (0.09)	227	0.52
4	9.775	7.912	0.993	0.254 (0.030)	0.246 (0.029)	1.587 (0.096)	4.606 (0.278)	3.11 (0.09)	4.47 (0.08)	155	0.91
5	21.738	8.811	1.098	0.464 (0.072)	0.423 (0.066)	2.859 (0.304)	8.437 (0.898)	4.20 (0.22)	5.38 (0.18)	144	0.53
6	28.156	6.397	1.094	0.221 (0.056)	0.196 (0.050)	2.790 (0.436)	3.641 (0.568)	4.39 (0.33)	5.62 (0.27)	121	0.55
7	21.244	5.677	0.928	0.116 (0.060)	0.103 (0.053)	1.353 (1.026)	1.993 (1.511)	2.65 (0.99)	4.11 (0.97)	67	0.89
8	21.738	7.675	1.029	0.268 (0.072)	0.242 (0.065)	1.794 (0.413)	4.413 (1.016)	3.50 (0.39)	4.82 (0.35)	42*	0.88
9	12.212	13.041	0.930	0.621 (0.056)	0.627 (0.057)	1.136 (0.056)	12.456 (0.617)	2.42 (0.06)	3.77 (0.06)	193	0.76
10	9.775	9.479	1.082	0.447 (0.045)	0.445 (0.045)	2.266 (0.096)	8.287 (0.349)	3.98 (0.08)	5.19 (0.07)	154	0.78

The X-ray observable of RXGCC clusters. The error are shown in the brackets.

† Parameters derived with scaling relation from the count rate. The quoted uncertainty refers to the 1σ error of the count rate at significant radius, together with the uncertainty of the scaling relation.

- The sum of the photon counts within the significant radius, with background photons subtracted. The [\*] symbol in this column labels out the case when the RASS tile fails to cover the whole area within the significant radius, which causes the under-estimation of the total photon number.

### 3.2. Parameter distributions

In this subsection, we discuss the distribution of X-ray observables of RXGCC clusters. Their distributions are shown in Fig. 4. The solid, dashed, dotted histograms demonstrate the parameter distribution of RXGCC sample, previous ICM-detected (*Bronze*) sample, and new ICM-detected (*Gold+Silver*) sample, while vertical lines show the corresponding median values. These median values are listed in Tab. 5. From the median values, it is clear that the

Table 5: The median parameter value for the new ICM-detected sample (*Gold+Silver*), the previous ICM-detected sample (*Bronze*), and the whole RXGCC sample. Both the  $F_{500}$  and  $L_{500}$  are the value in  $[0.1 - 2.4]$  keV band.

Parameter	Med. <sub>(G+S)</sub>	Med. <sub>(B)</sub>	Med. <sub>(RXGCC)</sub>
$R_{\text{sig}}$ [arcmin]	14.650	13.188	13.675
$R_{500}$ [arcmin]	8.534	9.726	9.273
$CR_{\text{sig}}$ [c/s]	0.148	0.276	0.234
$CR_{500}$ [c/s]	0.142	0.269	0.225
$F_{500}$ [ $10^{-12}$ erg/s/cm $^2$ ]	2.496	4.955	4.043
$L_{500}$ [ $10^{44}$ erg/s]	0.342	0.912	0.688
$M_{500}$ [ $10^{14}$ M $_{\odot}$ ]	1.246	2.270	1.843
$T_x$ [keV]	2.514	3.644	3.224
$\beta$	0.76	0.83	0.81

new ICM-detected clusters tend to have lower count rate, flux, luminosity, mass and temperature. Still, it is worth noting that the median flux of new ICM-detected clusters is close to the typical flux limit of previous RASS-based cluster catalogs ( $3 \times 10^{-12}$  erg/s/cm $^2$ ). Thus, a significant fraction of new ICM-detected clusters (*Gold+Silver*) have flux above it.

What is more important, the new ICM-detected sample has a lower median  $\beta$  value than the previous ICM-detected sample, shown in the last row of Tab. 5. The median  $\beta$  value of clusters in these two samples is 0.76 and 0.83, respectively. This is an indication for the new ICM-detected clusters to have generally flatter surface brightness profiles compared with previous ICM-detected clusters.

In the top panels of Fig. 5, the measured luminosity function and mass functions are shown. Note that we have not applied any correction of selection effects here – as a complete sample with accurate selection function would be required for this – so a quantitative comparison to previous catalogs, such as the REFLEX or HIFLUGCS samples, is not meaningful. In this plot, we show the cumulative number of RXGCC clusters above a specific value of luminosity or mass, as a very rough demonstration of the luminosity and mass function.

In bottom-left panel of Fig. 5, we show the cumulative number as a function of the X-ray flux (also called  $\log N$ - $\log S$  plot). In this plot, we overlay the dashed line with the slope of  $-1.5$  predicted by a static Euclidean universe with clusters uniformly distributed, which is a reasonable assumption for low-redshift clusters for a rough completeness check. This line is normalized to match it with the measurement at  $F_{500} = 2 \times 10^{-11}$  erg/s/cm $^{-2}$ . The theoretical line matches with our detection curve with  $F_{500} > 5 \times 10^{-12}$  erg/s/cm $^{-2}$ , shown with the vertical dotted line. This is a good indication that we have achieved a high completeness up to this flux, despite of our requirement of detecting significantly extended X-ray emission. A small bump at  $\sim 6 \times 10^{-11}$  erg/s/cm $^{-2}$  is worth to be noted, which likely stems from small number statistics and expected large cosmic variance at low redshift; i.e., we likely see large-scale structure here.

In addition, the relation between the redshift and luminosity are shown in the bottom-right panel, overlaid with the flux limit of  $10^{-12}$  and  $3 \times 10^{-12}$  erg/s/cm $^2$  as dotted curve and dashed curve, respectively. It is noted that there are 115 new ICM-detected RXGCC clusters with flux larger than the flux limit of REFLEX ( $3 \times 10^{-12}$  erg s $^{-1}$  cm $^{-2}$  in  $0.1 - 2.4$  keV band).

### 3.3. Comparison of radii, count rates, and flux

Firstly, we compare different radii (i.e., the significant radius,  $R_{500}$ , *extent*). As shown in the top panels of Fig. 6,  $R_{\text{sig}}$  is compared with  $R_{500}$  and *extent*, the definitions and estimation methods are described in Sec. 2.4.1 and Sec. 2.2. In the plot, it is clear that  $R_{\text{sig}}$  is larger than both  $R_{500}$  and *extent* in most cases. Since *extent* shows the core radius of the  $\beta$ -model, and  $R_{\text{sig}}$  demonstrates the region with significant X-ray emission, it is reasonable  $R_{\text{sig}}$  is larger in most cases. Given the low background of the ROSAT PSPC, the X-ray emission happens to spread beyond  $R_{500}$ . However, for some clusters we seem to detect emission out to  $\sim 3 - 5 \times R_{500}$ , which is surprising, at first sight. One possible reason is that our estimation is based on the assumption of the  $\beta$ -model with the typical value of  $\beta = 2/3$ , which does not necessarily describe properly the data, especially for the very extended clusters that we aim to discover. With a much flatter profile of  $\beta \ll 2/3$ , the very extended cluster has an X-ray emission extending up to a much larger area.

In addition, we compare the integrated count rate and flux within  $R_{\text{sig}}$  and  $R_{500}$ , respectively. This is shown in the bottom panels of Fig. 6. Compared to the top panels, these relations are much tighter. However, the conversion between the  $CR_{\text{sig}}$  and the  $CR_{500}$  are derived by assuming a typical cluster profile with  $\beta = 2/3$ , thus their relation is related to the relation between  $R_{500}$  and  $R_{\text{sig}}$ . The conversion between the  $CR_{500}$  and  $F_{500}$  is derived with the information of cluster redshift, ICM temperature, galactic absorption, and metallicity. The tight relations between the  $CR_{\text{sig}}$ ,  $CR_{500}$ , and  $F_{500}$  indicate the robustness of our parameter estimation method.

Furthermore, we separate the RXGCC sample into two sub-samples by the  $\beta$  value, and show the relation of the  $\beta$  value, the significant radius, the core radius, and the total photon count inside the significant radius in Fig. 7. The  $\beta$  value and  $r_c$  are estimated by fitting the growth curve with the  $\beta$ -model convolved with PSF as described in Sec. 2.4.2, and  $R_{\text{sig}}$  is derived from the growth curve as shown in Sec. 2.4.1. A smaller  $\beta$  value corresponds to a flatter emission profile. As shown in the bottom panel of Fig. 7, it seems there are two subsamples, thus we separate the RXGCC sample into 'high- $\beta$ ' and 'low- $\beta$ ' sample with  $\beta = 2/3$ , and show them with different symbols. Except for the value difference of  $\beta$ , these two subsamples do not show much difference in the core radius, photon number within the significant radius, and the relation between the significant radius and the core radius. The significant radius is larger than the core radius for most of detections.

Finally, we compare the same set of parameters for the *Silver + Bronze* sample (shown with solid dots) with the *Gold* sample (shown with empty circles and squares). As shown in Fig. 8, the later sample tends to have lower  $\beta$  value, which indicates their flat profile. We further divided the *Gold* sample into *Bright Gold* sample (shown with empty squares) and *Faint Gold* sample (shown with empty circles) by  $F_{500} = 3 \times 10^{-12}$  erg/s/cm $^2$ . Compared with the *Faint Gold* sample, the *Bright Gold* sample tend to have a much larger significant radius than the core radius, a larger number of photon within the significant radius, and a much flatter profile. Especially, in the  $\beta < 2/3$  regime, the *Bright Gold* sample has a much smaller  $\beta$  value (i.e., much flatter profile) than the *Faint Gold*. Thus, our detection ef-



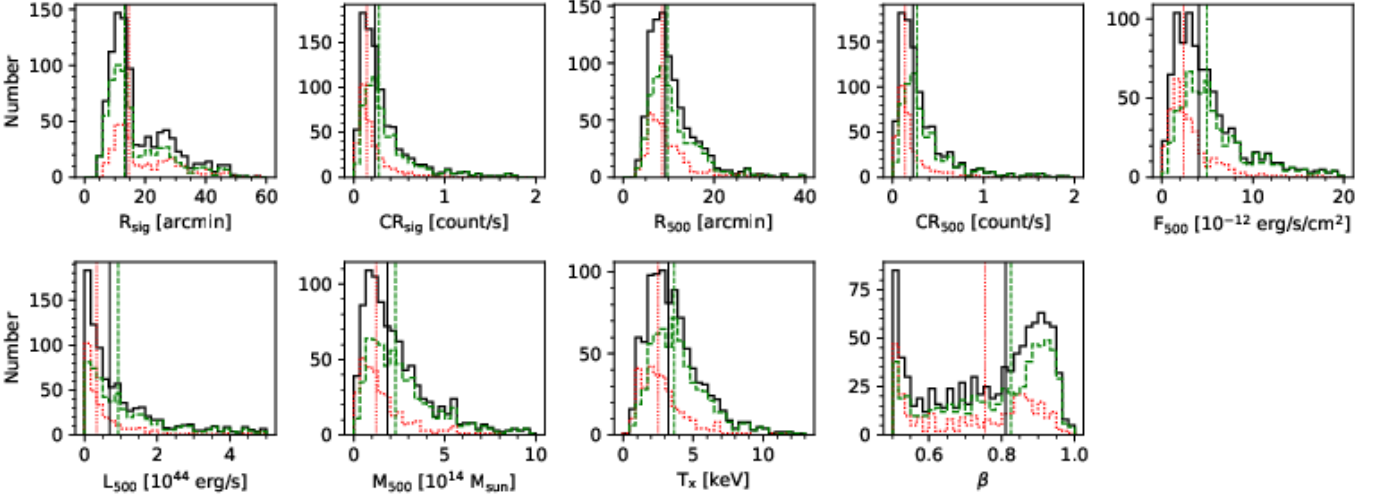


Fig. 4: The distribution of parameters of the RXGCC sample, previous ICM-detected sample (*Bronze*), and new ICM-detected sample (*Gold+Silver*), shown with solid, dashed, and dotted histograms and lines, in sequence. Refer to Sec. 2.4.1 for details about the estimation methods. Both the  $F_{500}$  and  $L_{500}$  are the value in  $[0.1 - 2.4]$  keV band. To show the main character, we ignore a few outliers with large parameter value in the histogram, and set manually the upper parameter limit of the axis in the plot.

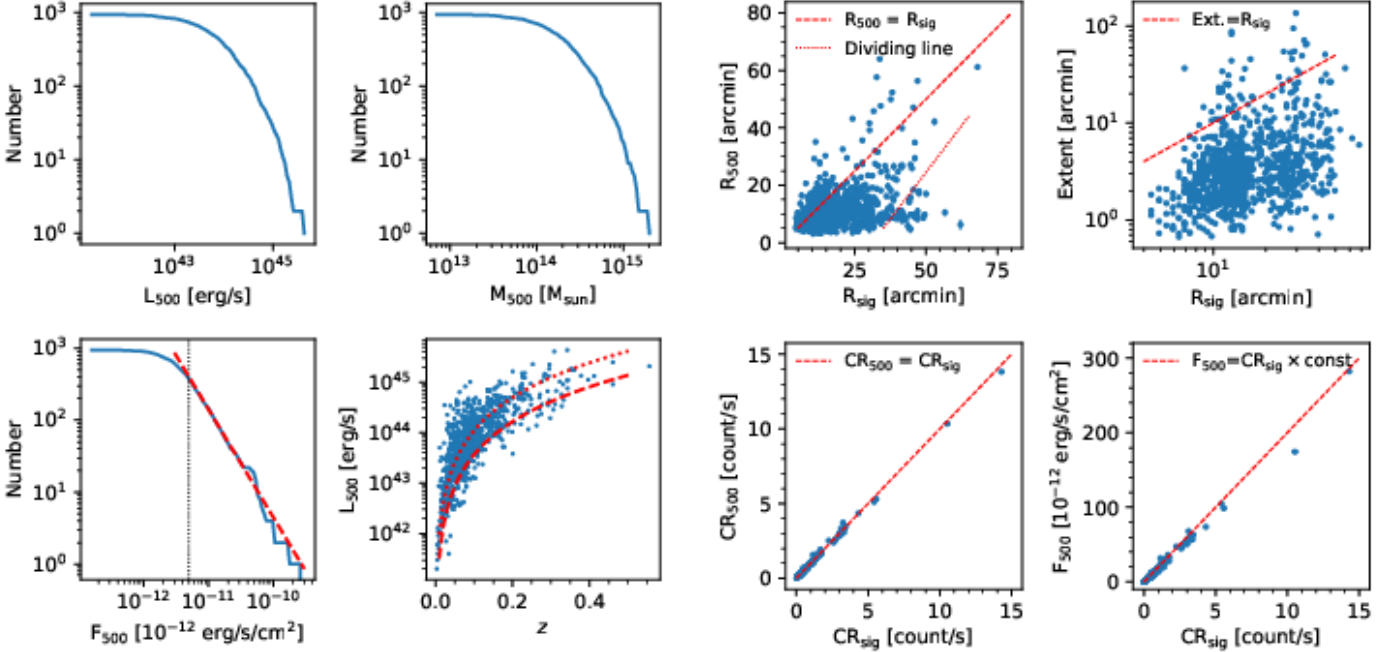


Fig. 5: In top-left, top-right, and bottom-left panels, we show the relation between the value of  $L_{500}$ ,  $M_{500}$ ,  $F_{500}$ , and the integrated cluster numbers with larger luminosity, mass, or flux. In the bottom-left panel, the dashed line has a slope of  $-1.5$ , normalized to match the value with  $f_x = 2 \times 10^{-11}$  erg/s/cm $^2$ . The dotted vertical line labels the flux of  $5 \times 10^{-12}$  erg/s/cm $^2$ . In the bottom-right panel, it shows the relation between the redshift and  $L_{500}$ . The curves for the flux limits of  $10^{-12}$  and  $3 \times 10^{-12}$  erg/s/cm $^2$  are overlapped as dotted curve and dashed curve, respectively. Both the  $F_{500}$  and  $L_{500}$  are the value in  $[0.1 - 2.4]$  keV band.

Fig. 6: The relation between the  $R_{500}$ ,  $R_{\text{sig}}$ ,  $\text{extent}$ , the integrated count rate within  $R_{500}$ , the integrated count rate within  $R_{\text{sig}}$ , and the flux inside  $R_{500}$ . In the top-left, top-right, and bottom-left panels, the red dashed line labels the 1:1 relation, while in the bottom-right panel it shows the relation of  $F_{500} = CR_{\text{sig}} \times 2 \times 10^{-11}$  (erg/s/cm $^2$ )/(count/s). In the top-left panel, the red dotted line shows the dividing line to get the very extended candidates discussed in Sec. 4.1.

efficiency of flat clusters is higher for the bright ones, which comes from the limitation of the telescope sensitivity. In another word, our detection of such flat clusters with shallow

RASS data shows that it is promising to use this algorithm to make detection of large number of very extended sources with deeper observation or the detector with better sensitivity.

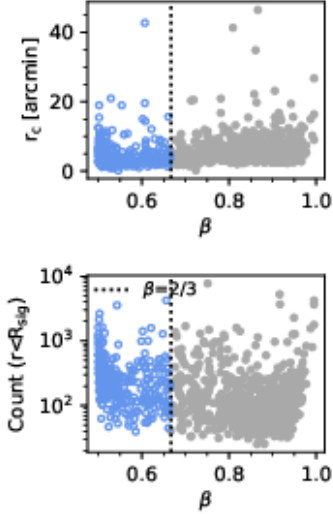


Fig. 7: The relation between the  $\beta$  value, the core radius ( $r_c$ ), the significant radius ( $R_{\text{sig}}$ ), and the total number of photons within the significant radius. The grey dots, and blue empty circles show the 'high  $\beta$ ' and 'low  $\beta$ ' samples, respectively, which are divided by the line of  $\beta = 2/3$ .

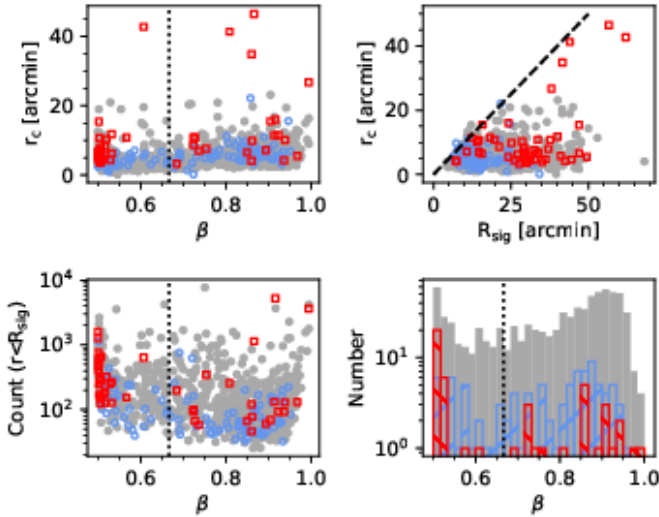


Fig. 8: Top-left, top-right, bottom-left panels are the same with Fig. 7, and only differs in symbols. In these panels, the grey dots, blue empty circles, and red empty squares represent the *Silver + Bronze* sample, *Faint Gold* sample, and *Bright Gold* sample, respectively. The *Bright Gold* and *Faint Gold* samples are divided from the *Gold* sample by  $F_{500} = 3 \times 10^{-12}$  erg/s/cm<sup>2</sup>. Bottom-right panel shows the  $\beta$  histogram of the same samples, with colors matching with other panels.

## 4. Discussion

### 4.1. Very extended candidates

In the top-left panel of Fig. 6, we show the relation between the significant radius ( $R_{\text{sig}}$ ) and  $R_{500}$ . We find  $R_{\text{sig}}$  tends to be larger than  $R_{500}$ . Thus, we separate out very

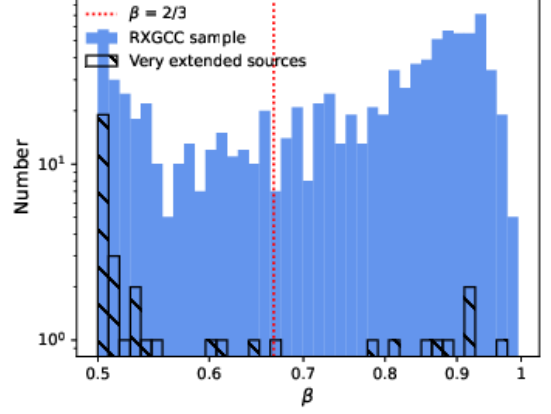


Fig. 9: The  $\beta$  distribution of the whole RXGCC and the very extended sub-sample. The very extended sub-sample comprise of clusters located at the bottom-right part of the dividing line in the top-left panel of Fig. 6.

extended clusters located at the bottom-right corner, using the dotted dividing line therein. The comparison of the  $\beta$  distribution of the whole RXGCC and this very extended sub-sample is shown in Fig. 9. Most of these extended candidates have  $\beta < 2/3$ , with a much flatter profile than the typical clusters. The detection of cluster candidates with such flat profiles demonstrates the efficiency of our algorithm and its possibility to detect much more extended clusters with forthcoming observations.

### 4.2. False detections

In our detections, except of 944 cluster candidates compiled into the RXGCC catalog, there are 364 false detections. There are several possible reasons for false detections, such as large variation of exposure time, background, or the column density of neutral hydrogen, contamination from foreground or background, clustering of X-ray point sources (stars or AGNs), projection overlapping of outskirts of nearby bright/extended X-ray sources, or projection overlapping of high-redshift clusters.

The spatial distribution of false detections is shown with red dots in the bottom panel of Fig. 3. The ratio of false detections in our detection is 27.8%. Most of them are located at the ecliptic poles and along ecliptic longitudes, where the exposure variation is large (shown at the second panel of Fig. 10). The exposure variation is taken from the difference between the highest and lowest exposure time of pixels in  $1^\circ \times 1^\circ$  region and divided by the median value. The way of RASS scanning causes large exposure variation at the direction vertical to the scanning direction, shown in the top panel of Fig. 10, which is adopted from the Fig. 1 of Voges et al. (1999). The spatial correlation in the top and the second panel indicates that large exposure variation is one reason for the false detections.

In the third panel of Fig. 10, we plot the histogram of exposure variation for detections in classes. It is clear the average exposure variation of *False detections* is higher than other classes and the whole detection sample. In the bottom panel of Fig. 10, it shows the positive correlation between the false detection ratio with the exposure varia-

tion. Therefore, we take the large exposure variation as the main reason for false detections.

#### 4.3. Cross-match RXGCC with representative ICM-detected cluster catalogs

In this section, we discuss the robustness of cross-matching criteria in the catalog cross-matching, as described in Sec. 2.3.3. These cross-matching criteria, offset  $< 15'$  & offset  $< 0.5$  Mpc &  $\Delta z < 0.01$ , are used for all cross-matching in this work.

Thus, we cross-match the RXGCC catalog with four representative ICM-detected cluster catalogs. We consider two ROSAT-based X-ray cluster catalogs, the ROSAT-ESO flux limited X-ray catalog (REFLEX, Böhringer et al. 2004) and the northern ROSAT all-sky catalog (NORAS, Böhringer et al. 2000), as well as the MCXC and PSZ2 catalogs to represent large cluster catalogs in X-ray and microwave bands. Firstly, we consider all matches with offset  $< 1$  degree, and show the offset distribution. Secondly, we constrain the offset within  $15'$ , and show the redshift difference of matches. The result is shown in Fig. 11. When the offset increases, the number of matching pairs decreases firstly, and increases later for the random distribution and projection effect. Similarly, with the redshift difference increases, the number of matching pairs has an exponential decrease, and a tiny increase later. The criteria labeled with dotted vertical lines are used in our work to ensure a high probability for a physical correlation of matched clusters and a low probability of projection effects.

#### 4.4. Known X-ray sources

In this section, we cross-match the RXGCC catalog with the ROSAT X-ray Source Catalog (RXS, Voges et al. 1999, 2000; Boller et al. 2016). The RXS is often used as the underlying resource of possible X-ray clusters (e.g., Böhringer et al. 2000, 2004). So, in case of RXGCC clusters not included in the RXS, they will be missed by all cluster searching projects which take the RXS catalog as input. The ratio of RXGCC clusters with RXS detection in  $5'$  is 91.1%, as shown in Fig. 12. That is, there are 84 clusters without any RXS sources within  $5'$ . These clusters are definitely missed by X-ray cluster detection projects starting from the RXS sources.

## 5. Conclusion

In this project, we set out to reanalyze the RASS in the  $[0.5 - 2.0]$  keV band and search for possibly missed X-ray clusters. With the wavelet filtering, source extraction, and maximum likelihood fitting, we make 1308 detections. Combining the RASS images with optical, infrared, microwave band images, the neutral hydrogen distribution, and the spatial and redshift distribution of galaxies in the field, we identify 944 clusters and remove other false detections. Among these clusters, there are 149 ones detected for the first time, and additional 154 ones detected through the ICM emission for the first time. For each candidate, we estimate the redshift using the distribution of the spectroscopic and photometric redshift of galaxies, and use the growth curve analysis to estimate the parameters, such as count rate, flux, luminosity and mass.

115 of the 149 + 154 clusters detected here with ICM emission for the first time have fluxes  $> 3 \times 10^{-12}$  erg/s/cm<sup>2</sup>; i.e., above the rough flux limits applied in previous RASS cluster catalogs. We find that the new clusters deviate in their properties from the previously known cluster population. In particular, the new clusters have flatter surface brightness profiles, which makes their detection more difficult with detection algorithms optimized for point sources. This new cluster population now needs to be followed up with deep pointed observations with XMM-Newton and Chandra in order to determine their properties in more detail. After that, it allows us to estimate the magnitude of any potential bias in the estimated completeness of previous surveys, as well as its impact on  $\Omega_M$  and  $\sigma_8$  constraints. Furthermore, these findings will help the upcoming cluster searches with eROSITA data.

*Acknowledgements.* We acknowledge support from the National Key R&D Program of China (2016YFA0400703) and the National Science Foundation of China (11721303, 11890693). The authors wish to thank Angus Wright, Jens Erler, Cosmos C. Yeh, Chaoli Zhang, Aiyuan Yang, Linhua Jiang, Zhonglue Wen, and Jinlin Han for useful help and discussions during the development of this paper. The authors thank the support from the CAS-DAAD Joint Fellowship Programme for Doctoral Students of Chinese Academy of Sciences (ST 34). WX acknowledges the support of the Chinese Academy of Sciences through grant No. XDB23040100 from the Strategic Priority Research Program and that of the National Natural Science Foundation of China with grant No. 11333005. We acknowledge support from the Chinese Academy of Sciences (CAS) through a China-Chile Joint Research Fund #1503 administered by the CAS South America Center for Astronomy.

## References

- Abbott, T. M. C., Abdalla, F. B., Alarcon, A., et al. 2018, *Phys. Rev. D*, 98, 043526
- Abbott, T. M. C., Aguena, M., Alarcon, A., et al. 2020, *Phys. Rev. D*, 102, 023509
- Abell, G. O. 1958, *ApJS*, 3, 211
- Abell, G. O., Corwin, Jr., H. G., & Olowin, R. P. 1989, *ApJS*, 70, 1
- Allen, S. W., Evrard, A. E., & Mantz, A. B. 2011, *ARA&A*, 49, 409
- Allen, S. W., Rapetti, D. A., Schmidt, R. W., et al. 2008, *MNRAS*, 383, 879
- Bertin, E. & Arnouts, S. 1996, *A&AS*, 117, 393
- Bilicki, M., Jarrett, T. H., Peacock, J. A., Cluver, M. E., & Steward, L. 2014, *ApJS*, 210, 9
- Bleem, L. E., Stalder, B., de Haan, T., et al. 2015, *ApJS*, 216, 27
- Böhringer, H., Chon, G., Retzlaff, J., et al. 2017, *AJ*, 153, 220
- Böhringer, H., Schuecker, P., Guzzo, L., et al. 2004, *A&A*, 425, 367
- Böhringer, H., Schuecker, P., Guzzo, L., et al. 2001, *A&A*, 369, 826
- Böhringer, H., Voges, W., Huchra, J. P., et al. 2000, *ApJS*, 129, 435
- Boller, T., Freyberg, M. J., Trümper, J., et al. 2016, *A&A*, 588, A103
- Borgani, S., Rosati, P., Tozzi, P., et al. 2001, *ApJ*, 561, 13
- Cash, W. 1979, *ApJ*, 228, 939
- Cavaliere, A. & Fusco-Femiano, R. 1976, *A&A*, 49, 137
- Clerc, N., Kirkpatrick, C. C., Finoguenov, A., et al. 2020, *MNRAS*, 497, 3976
- Clerc, N., Merloni, A., Zhang, Y. Y., et al. 2016, *MNRAS*, 463, 4490
- Clerc, N., Sadibekova, T., Pierre, M., et al. 2012, *MNRAS*, 423, 3561
- Craddace, R., Voges, W., Böhringer, H., et al. 2002, *ApJS*, 140, 239
- Dahle, H. 2006, *ApJ*, 653, 954
- Dunkley, J., Komatsu, E., Nolta, M. R., et al. 2009, *ApJS*, 180, 306
- Ebeling, H., Edge, A. C., Allen, S. W., et al. 2000, *MNRAS*, 318, 333
- Ebeling, H., Edge, A. C., Böhringer, H., et al. 1998, *MNRAS*, 301, 881
- Ebeling, H., Edge, A. C., & Henry, J. P. 2001, *ApJ*, 553, 668
- Ebeling, H., Voges, W., Böhringer, H., et al. 1996, *MNRAS*, 281, 799
- Ebeling, H. & Wiedenmann, G. 1993, *Phys. Rev. E*, 47, 704
- Erler, J., Basu, K., Chluba, J., & Bertoldi, F. 2018, *MNRAS*, 476, 3360
- Faccioli, L., Pacaud, F., Sauvageot, J. L., et al. 2018, *A&A*, 620, A9
- Finoguenov, A., Rykoff, E., Clerc, N., et al. 2020, *A&A*, 638, A114
- Ghirardini, V., Bulbul, E., Hoang, D. N., et al. 2021, *A&A*, 647, A4

- Hasselfield, M., Hilton, M., Marriage, T. A., et al. 2013, *J. Cosmology Astropart. Phys.*, 7, 008
- Henry, J. P., Mullis, C. R., Voges, W., et al. 2006, *ApJS*, 162, 304
- HI4PI Collaboration, Ben Bekhti, N., Flöer, L., et al. 2016, *A&A*, 594, A116
- Hilton, M., Hasselfield, M., Sifón, C., et al. 2018, *ApJS*, 235, 20
- Kirkpatrick, C. C., Clerc, N., Finoguenov, A., et al. 2021, *MNRAS*, 503, 5763
- Kowalski, M., Rubin, D., Aldering, G., et al. 2008, *ApJ*, 686, 749
- Kravtsov, A. V. & Borgani, S. 2012, *ARA&A*, 50, 353
- Ledlow, M. J., Voges, W., Owen, F. N., & Burns, J. O. 2003, *AJ*, 126, 2740
- Liu, T., Tozzi, P., Tundo, E., et al. 2015, *ApJS*, 216, 28
- Lloyd-Davies, E. J., Romer, A. K., Mehtens, N., et al. 2011, *MNRAS*, 418, 14
- Marriage, T. A., Acquaviva, V., Ade, P. A. R., et al. 2011, *ApJ*, 737, 61
- Mehtens, N., Romer, A. K., Hilton, M., et al. 2012, *MNRAS*, 423, 1024
- Merloni, A., Nandra, K., & Predehl, P. 2020, *Nature Astronomy*, 4, 634
- Merloni, A., Predehl, P., Becker, W., et al. 2012, *arXiv e-prints*, arXiv:1209.3114
- Mukai, K. 1993, *Legacy*, 3, 21
- Mullis, C. R., McNamara, B. R., Quintana, H., et al. 2003, *ApJ*, 594, 154
- Oguri, M. 2014, *MNRAS*, 444, 147
- Oguri, M., Lin, Y.-T., Lin, S.-C., et al. 2018, *PASJ*, 70, S20
- Pacaud, F., Clerc, N., Giles, P. A., et al. 2016, *A&A*, 592, A2
- Pacaud, F., Pierre, M., Refregier, A., et al. 2006, *MNRAS*, 372, 578
- Pedersen, K. & Dahle, H. 2007, *ApJ*, 667, 26
- Perlman, E. S., Horner, D. J., Jones, L. R., et al. 2002, *ApJS*, 140, 265
- Piffaretti, R., Arnaud, M., Pratt, G. W., Pointecouteau, E., & Melin, J.-B. 2011, *A&A*, 534, A109
- Pillepich, A., Porciani, C., & Reiprich, T. H. 2012, *MNRAS*, 422, 44
- Pillepich, A., Reiprich, T. H., Porciani, C., Borm, K., & Merloni, A. 2018, *MNRAS*, 481, 613
- Planck Collaboration, Ade, P. A. R., Aghanim, N., et al. 2016, *A&A*, 594, A27
- Planck Collaboration, Aghanim, N., Akrami, Y., et al. 2020a, *A&A*, 641, A1
- Planck Collaboration, Aghanim, N., Akrami, Y., et al. 2020b, *A&A*, 641, A6
- Pratt, G. W., Arnaud, M., Biviano, A., et al. 2019, *Space Sci. Rev.*, 215, 25
- Predehl, P., Andritschke, R., Arefiev, V., et al. 2020, *arXiv e-prints*, arXiv:2010.03477
- Reichert, A., Böhringer, H., Fassbender, R., & Mühlegger, M. 2011, *A&A*, 535, A4
- Reiprich, T. H., Basu, K., Ettori, S., et al. 2013, *Space Sci. Rev.*, 177, 195
- Reiprich, T. H. & Böhringer, H. 2002, *ApJ*, 567, 716
- Reiprich, T. H., Veronica, A., Pacaud, F., et al. 2021, *A&A*, 647, A2
- Rines, K., Diaferio, A., & Natarajan, P. 2007, *ApJ*, 657, 183
- Rosati, P., Della Ceca, R., Burg, R., Norman, C., & Giacconi, R. 1995, *ApJ*, 445, L11
- Rykoff, E. S., Rozo, E., Busha, M. T., et al. 2014, *ApJ*, 785, 104
- Rykoff, E. S., Rozo, E., Hollowood, D., et al. 2016, *ApJS*, 224, 1
- Scharf, C. A., Ebeling, H., Perlman, E., Malkan, M., & Wegner, G. 1997, *ApJ*, 477, 79
- Schellenberger, G. & Reiprich, T. H. 2017, *MNRAS*, 471, 1370
- Seljak, U. 2002, *MNRAS*, 337, 769
- Sunyaev, R. A. & Zeldovich, I. B. 1980, *ARA&A*, 18, 537
- Sunyaev, R. A. & Zeldovich, Y. B. 1970, *Comments on Astrophysics and Space Physics*, 2, 66
- Sunyaev, R. A. & Zeldovich, Y. B. 1972, *Comments on Astrophysics and Space Physics*, 4, 173
- Takey, A., Durret, F., Mahmoud, E., & Ali, G. B. 2016, *A&A*, 594, A32
- Takey, A., Schwobe, A., & Lamer, G. 2011, *A&A*, 534, A120
- Takey, A., Schwobe, A., & Lamer, G. 2013, *A&A*, 558, A75
- Takey, A., Schwobe, A., & Lamer, G. 2014, *A&A*, 564, A54
- Tarrío, P., Melin, J. B., & Arnaud, M. 2018, *A&A*, 614, A82
- Tarrío, P., Melin, J. B., & Arnaud, M. 2019, *A&A*, 626, A7
- Truemper, J. 1992, *QJRAS*, 33, 165
- Truemper, J. 1993, *Science*, 260, 1769
- Valtchanov, I., Pierre, M., & Gastaud, R. 2001, *A&A*, 370, 689
- Viana, P. T. P., Nichol, R. C., & Liddle, A. R. 2002, *ApJ*, 569, L75
- Vikhlinin, A., McNamara, B. R., Forman, W., et al. 1998, *ApJ*, 502, 558
- Voges, W., Aschenbach, B., Boller, T., et al. 1999, *A&A*, 349, 389
- Voges, W., Aschenbach, B., Boller, T., et al. 2000, *IAU Circ.*, 7432
- Wen, Z. L. & Han, J. L. 2015, *ApJ*, 807, 178
- Wen, Z. L., Han, J. L., & Liu, F. S. 2010, *MNRAS*, 407, 533
- Wen, Z. L., Han, J. L., & Liu, F. S. 2012, *ApJS*, 199, 34
- Wen, Z. L., Han, J. L., & Yang, F. 2018, *MNRAS*, 475, 343
- Xu, W., Ramos-Ceja, M. E., Pacaud, F., Reiprich, T. H., & Erben, T. 2018, *A&A*, 619, A162
- Zwicky, F. & Kowal, C. T. 1968, “Catalogue of Galaxies and of Clusters of Galaxies”, Volume VI (“Pasadena: California Institute of Technology“)

## Appendix A: Method comparison with Paper I

Compared with Paper I, there are some changes in the method.

- 1. The 40 cluster candidates in [Takey et al. \(2016\)](#) are discarded since they do not provide spectroscopic redshift estimations. The [Wen et al. \(2012\)](#) was updated in [Wen & Han \(2015\)](#), and the updated catalog is used in this work. The X-ray clusters in [Wen et al. \(2018\)](#) are not considered as ICM-detected clusters, because they are detected with optical and infrared data. In addition, more recent published X-ray cluster catalogs are taken into account.
- 2. The galaxy redshift is constrained to the range  $0 < z < 0.4$ . Since the depth of RASS makes it difficult to detect the X-ray emission from extended clusters at higher redshift. The inclusion of high redshift galaxies will bring unnecessary contamination for the redshift determination.
- 3. The cross-matching with previously identified clusters is performed with the offset both  $< 0.5$  Mpc and  $< 15'$ , instead of  $< 15'$  in Paper I. This comes from the physical size corresponding to  $15'$  varies largely with the redshift, which can be largely different from the typical cluster size. Thus, the previous offset threshold casts doubt on the validity of the corresponding cross-matching, and further classification.
- 4. The spectroscopic and photometric redshifts of galaxies are combined, instead of taken separately in Paper I, to make the redshift estimation. This comes from the fact that the combination of galaxy redshift information provide a more accurate estimation, especially in the area with only a limited number of spectroscopic galaxy redshift are available.

## Appendix B: Estimation of contamination ratio

Optical and infrared cluster catalogues contain larger number of objects in comparison with ICM-based cluster catalogues. In our classification, the cross-matching of our detections with previous optical/infrared-identified clusters might result in mis-identification due to projection effects. Taking the catalog from [Wen et al. \(2012\)](#) as an example, there are 132 684 clusters identified within the SDSS-III area of 14 000 deg<sup>2</sup>. That is, there is on average  $\sim 1$  cluster in the circular area with the radius of 11 arcmin. And 11 arcmin is  $\sim 1$  Mpc for a cluster with  $z = 0.0770$ , which is the median redshift of the RXGCC sample. This means, at least in some area (e.g., within the SDSS coverage), there

is on average one optical cluster within an area with the size of a typical cluster. Although our algorithm of redshift determination and visual check will help to remove much of this kind of contamination, some contamination is expected to exist.

To estimate the contamination ratio from the projection effect, we make 200 simulations. In each simulation, there are 1100  $\sim$  1200 positions taken randomly with the Aitoff projection. We also discard some areas from the whole sky, as described in Sec. 2.1. Then, we classify them by cross-matching them with previous-identified clusters, as described in Sec. 2.3.2. The classification criteria in Sec. 2.3.3 are taken, while no visual check is used for these simulation detections. In each simulation, the contamination number and ratio are normalized to 1308 total detections.

In Fig. B.1, we show simulation results. The upper limit of galaxy redshift is set to be 0.3 and 0.4 (shown with solid and dashed lines respectively in the figure), to remove the contamination from the high redshift galaxies in deep surveys, which is unlikely to detect with RASS. Additionally, the redshift of galaxies are taken in three different ways. Firstly, only spectroscopic redshift of galaxies is taken to make redshift estimation (shown with thin lines). Secondly, both the spectroscopic redshift and photometric redshift of galaxies are taken separately (shown with lines in the normal width). Thirdly, both the spectroscopic redshift and photometric redshift of galaxies are taken combined (shown with thick lines). This way, we get the detection number (shown with black lines), and the corresponding contamination ratio (shown with the blue lines) in simulations. They vary with the offset threshold (shown as the X-axis) in classes.

From the figure, the best criteria are obtained for a low contamination ratio and a high detection number. Thus, both the spectroscopic and photometric redshifts of galaxies are combined to derive the candidate redshift when  $0 < z < 0.4$ , and 0.5 Mpc & 15 arcmin is set as offset threshold when cross-matching the detections with previous-identified clusters. This way, the contamination ratio for ICM-detected clusters and optical/infrared-identified clusters obtained, as 0.008 and 0.100, respectively.

### Appendix C: Comparison of detected and undetected MCXC, PSZ2, Abell clusters

In this section, we compare the spatial and redshift distribution of detected and undetected MCXC, PSZ2, Abell clusters, as shown in Fig. C.1. In left panels, we show the detected and undetected MCXC, PSZ2, and Abell clusters in black dots and blue empty circles, respectively. We hold that our algorithm has no spatial preference, except for the high detection efficiency in the ecliptic poles. In right panels, the redshift distribution of detected and undetected MCXC, PSZ2, and Abell clusters are shown. It is obvious the detection efficiency peaks at  $z \sim 0.1$  and decreases largely with  $z > 0.2$ , except for the result of Abell clusters, which is limited by the catalog itself.

Therefore, our missing of these clusters likely comes from the restraints of the RASS observation. The data for MCXC includes not only RASS observations, but also ROSAT pointings with larger exposure times, which is vital for the detection of fainter clusters at high redshift. In

addition, the SZ effect in microwave band is a more efficient indicator for clusters at high redshift. However, the aim of this work is to detect missed very extended clusters, instead of a complete cluster catalog.

### Appendix D: Parameter comparison of detected and undetected REFLEX and NORAS clusters

In Fig. D.1 and Fig. D.2, we show the distribution of the redshift, radius, flux, and luminosity for detected and undetected REFLEX and NORAS clusters. Compared with undetected REFLEX/NORAS clusters, the detected clusters tend to have lower redshift, large size, brighter flux, and lower X-ray luminosity (i.e. lower mass).

### Appendix E: Examples

There are 60 clusters with  $extent > 15'$  in our catalog. For some of the detections, the  $extent$  might be over-estimated. This mainly comes from the effects of the foreground or background, or the fluctuation of the exposure map. However, this effect can be corrected with the growth curve analysis (Sec. 2.4.1). And the  $R_{500}$  is more accurate to characterize the cluster.

In Fig. E.1, the images of two such clusters are shown as examples. Both of them are with  $extent > 15'$ . The left column is RXGCC 296, and the right column is RXGCC 400. RXGCC 296 is a *Bronze* cluster, and RXGCC 400 is a *Silver* cluster. In each column, the RASS image, reconstructed X-ray image, DES image, SDSS images, and the redshift histogram of galaxies are shown in the sequence. As mentioned in Sec. 2.2,  $extent$  is an indication of the size of detected clusters, which is shown with the red circle in the first two panels of each column.

### Appendix F: Redshift and classification change in the catalog

In this section, we add comments about the redshift and classification changes for some detections, listed in the Tab. F.1. The automatic result of the redshift and classification are listed in last two columns, as the method described in Sec. 2.3.1, Sec. 2.3.2, and Sec. 2.3.3. As discussed in Sec. 2.3.4, the visual check resulted in modifications for some candidates, shown in the column 2 and 3, with the information of multi-wavelength images, spatial distribution and redshift of galaxies.

Table F.1: Redshift or classification changes.

RXGCC	$z$	C	$z$ (auto)	C (auto)	RXGCC	$z$	C	$z$ (auto)	C (auto)
27	0.0557	S	0.0800	B	637	0.1012	G	0.0315	S
48	0.2625	G	0.1537	S	644	0.0625	G	0.1349	B
51	0.2300	B	0.0000	F	649	0.0312	S	0.0688	B
68	0.1630	S	0.0000	F	654	0.2701	S	0.0811	G
86	0.0694	B	0.1235	B	659	0.2647	B	0.2957	G
87	0.0170	S	0.0728	B	662	0.1668	B	0.0000	F
97	0.1175	B	0.0653	G	668	0.2060	B	0.0229	G
99	0.3416	B	0.0000	F	695	0.0803	G	0.1109	G
100	0.1700	B	0.0000	F	703	0.1306	B	0.0627	G
103	0.2198	B	0.1846	G	704	0.1603	B	0.0000	F
111	0.2818	B	0.0000	F	706	0.1377	S	0.3383	G
119	0.0989	G	0.0519	G	716	0.2410	S	0.1090	G
121	0.1290	G	0.0707	G	717	0.1035	S	0.0842	G
131	0.2700	B	0.0000	F	718	0.2265	G	0.1089	G
162	0.1441	S	0.0639	G	722	0.3059	B	0.0000	F
178	0.1039	B	0.0742	G	732	0.1406	B	0.0000	F
182	0.2252	G	0.0000	F	734	0.1000	G	0.0466	G
197	0.2000	B	0.0773	G	739	0.1790	B	0.0000	F
205	0.1516	G	0.1388	G	740	0.1410	B	0.1152	G
207	0.2839	B	0.0330	S	742	0.1565	B	0.0000	F
208	0.0310	G	0.0720	G	743	0.3100	B	0.0647	G
210	0.2977	G	0.0000	F	744	0.3280	B	0.0000	F
220	0.1277	B	0.0515	S	750	0.2263	B	0.0586	G
229	0.4600	B	0.0000	F	767	0.0924	G	0.0487	G
232	0.0977	G	0.0628	G	773	0.2764	B	0.0000	F
237	0.4600	B	0.0000	F	774	0.1790	B	0.0000	F
266	0.1750	B	0.0000	F	777	0.2006	S	0.0000	F
276	0.0222	B	0.0615	B	779	0.1080	B	0.0913	S
306	0.4118	B	0.0897	G	782	0.1680	B	0.0162	G
307	0.0941	G	0.0264	S	783	0.2057	B	0.0900	G
323	0.1381	S	0.1216	S	784	0.1623	B	0.0000	F
326	0.1535	B	0.1272	G	797	0.0928	B	0.0715	S
338	0.2060	B	0.1367	G	799	0.2103	B	0.0000	F
341	0.1193	G	0.3051	G	805	0.1886	B	0.0000	F
346	0.1087	G	0.0206	S	807	0.2371	B	0.0000	F
354	0.0410	S	0.1190	G	812	0.1044	G	0.0825	G
384	0.2480	G	0.0765	G	822	0.2746	B	0.0000	F
401	0.1066	S	0.0705	B	833	0.1419	S	0.0593	G
421	0.3081	G	0.0508	S	836	0.0494	B	0.0703	G
496	0.2953	S	0.0554	G	854	0.1402	G	0.0000	F
570	0.2440	G	0.0986	G	919	0.0286	B	0.1867	S
579	0.1158	B	0.1003	G	926	0.1700	G	0.0466	G
590	0.5551	B	0.3386	G	937	0.2478	G	0.0855	G
596	0.2226	B	0.0000	F					

Note. The 2nd and 3rd columns are the estimated redshift and classification listed in the RXGCC catalog. The 4th and 5th columns are the redshift and classes obtained with methods in Sec. 2.3.1, Sec. 2.3.2, and Sec. 2.3.3, before the visual inspection discussed in Sec. 2.3.4.

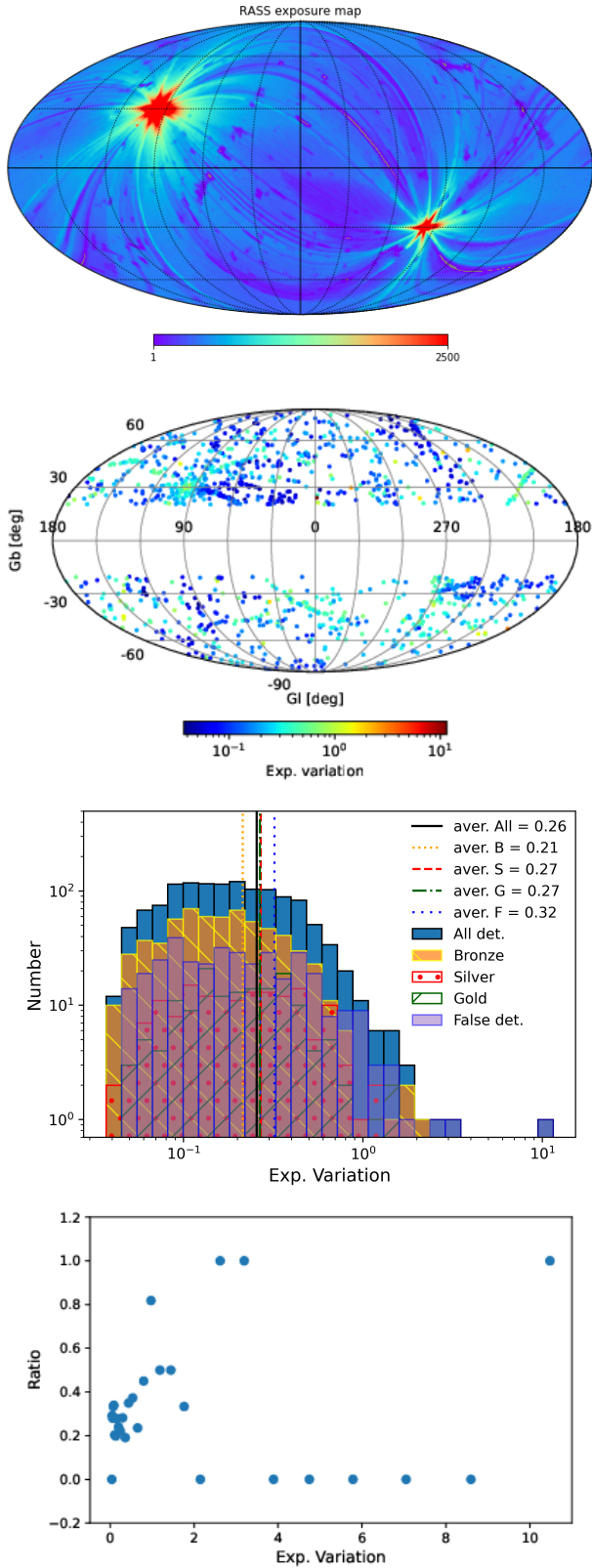


Fig. 10: Top panel: the RASS-II exposure map (adapted from the Fig. 1 of *Voges et al. 1999*.) Second panel: all-sky distribution of all detections, colors vary with the exposure variation. Third panel: the exposure variation distribution for detections in classes, the average value are overlaid with vertical lines. Bottom panel: the relation between the false detection ratio with exposure variation.

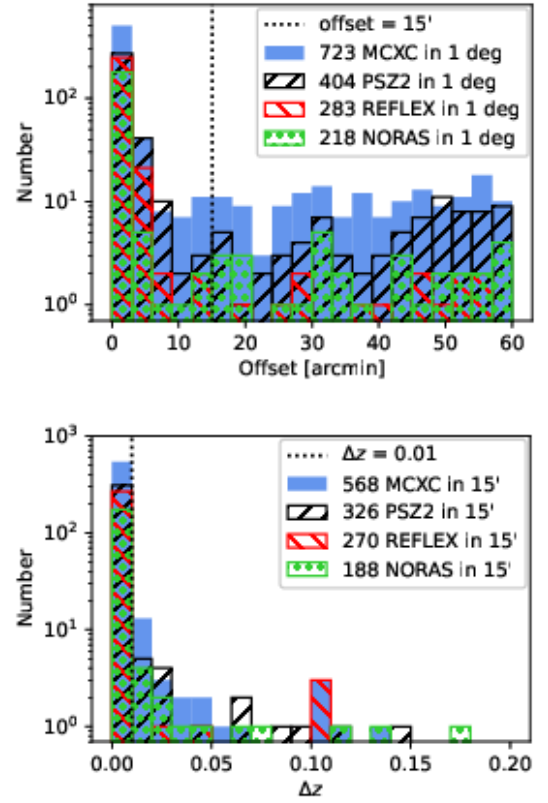


Fig. 11: The difference of positions and redshifts between our candidates and position-matched MCXC/PSZ2/REFLEX/NORAS clusters. In the top panel, the offset threshold is set as 1 degree, without setting redshift limit. In the bottom panel, the position offset is set as  $< 15'$ . The dotted vertical lines labels out the criteria used in this work.

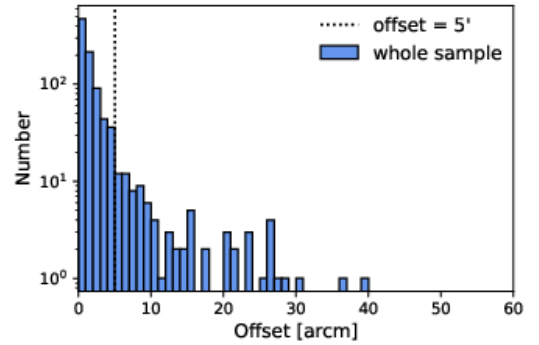


Fig. 12: The offset distribution between RXGCC clusters and the nearest RXS source.

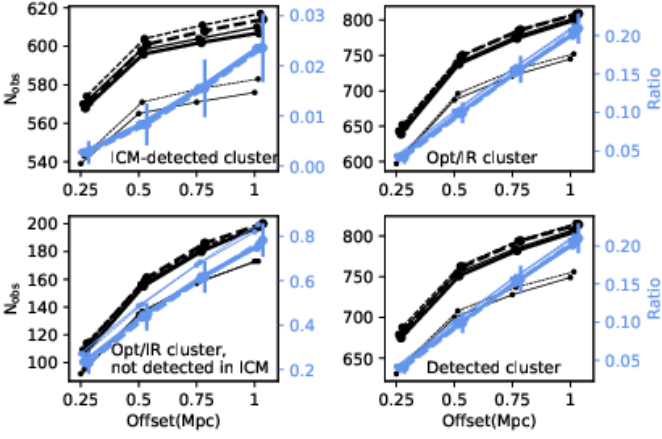


Fig. B.1: The number of detections (shown as black line with labels on the left) and contamination ratio (shown as blue line with labels on the right) varies with the offset threshold in the cross-matching with previously identified clusters (shown in X-axis). The offset has been set to be 0.25, 0.5, 0.75, 1.0 Mpc. The dots in the plot are shifted to the right with a little distance to avoid the overlapping. The detection numbers and contamination ratio for previous ICM-detected clusters (top-left panel), previous optical/infrared clusters (top-right panel), previous optical/infrared clusters not detected in ICM (bottom-left panel), the whole sample of detections (bottom-right panel) are shown. The solid and dashed lines shows the results when the upper limit of galaxy redshift is set to be 0.3 and 0.4, respectively. To estimate the redshift of detections, we consider three different situations. Firstly, we only take spectroscopic galaxy redshift into account (shown with thin lines). Secondly, we consider the spectroscopic galaxy redshift and photometric one separately (shown with lines in the normal width). Lastly, we combine the spectroscopic galaxy redshifts and photometric ones together without distinguishing them (shown with thick lines).



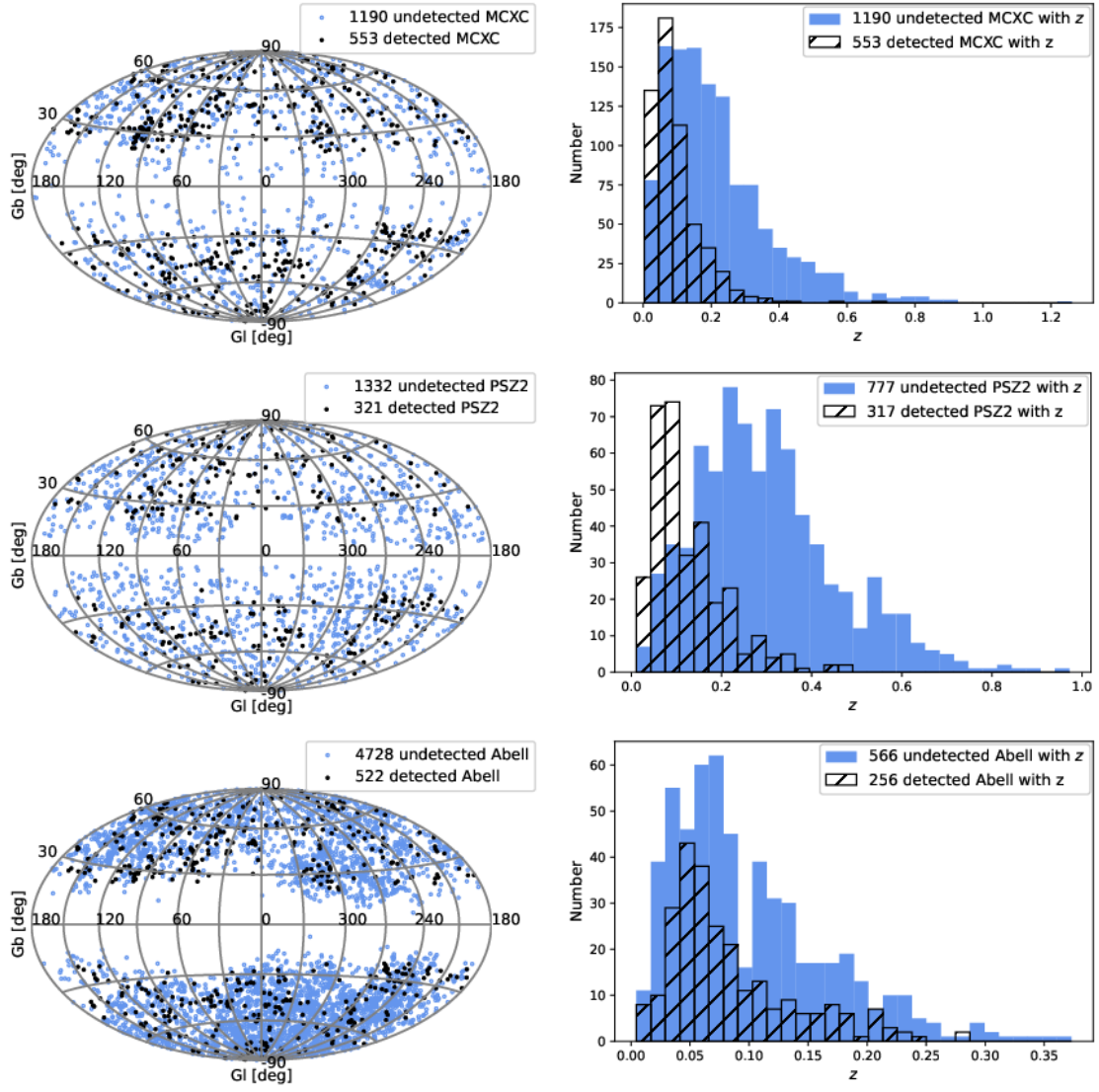


Fig. C.1: Comparison of spatial distribution (left panels) and redshift distribution (right panels) of detected and undetected MCXC, PSZ2 and Abell clusters, from the top to the bottom panels.

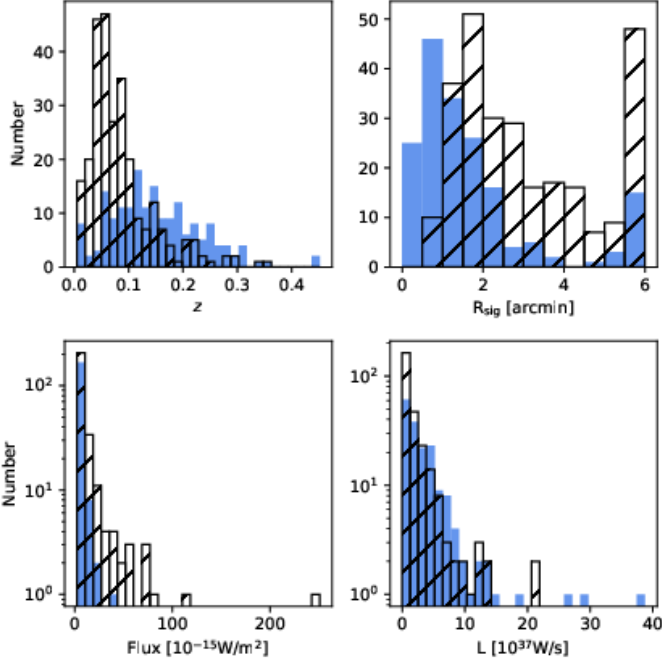


Fig. D.1: The distribution of the redshift, significant radius, flux, luminosity for detected and undetected REFLEX clusters. The histogram filled with slash lines is for the detected clusters, while the blue filled histogram for the undetected ones.

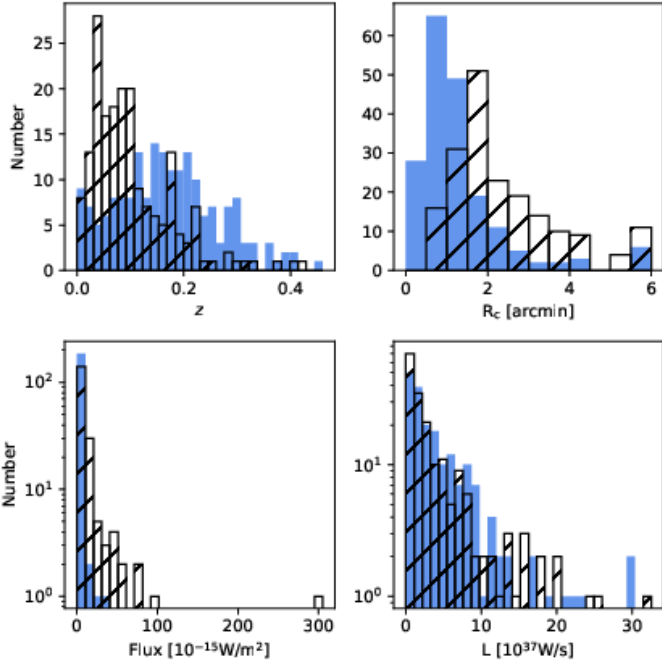


Fig. D.2: The distribution of the redshift, core radius, flux, luminosity for detected and undetected NORAS clusters. The histogram filled with slash lines is for the detected clusters, while the blue filled histogram for the undetected ones.

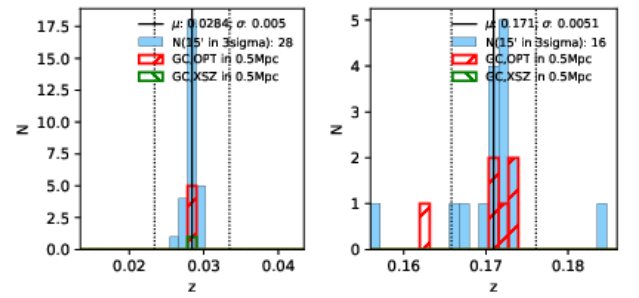
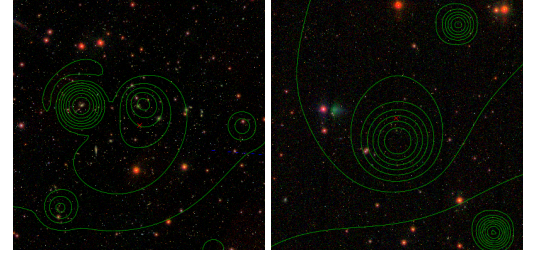
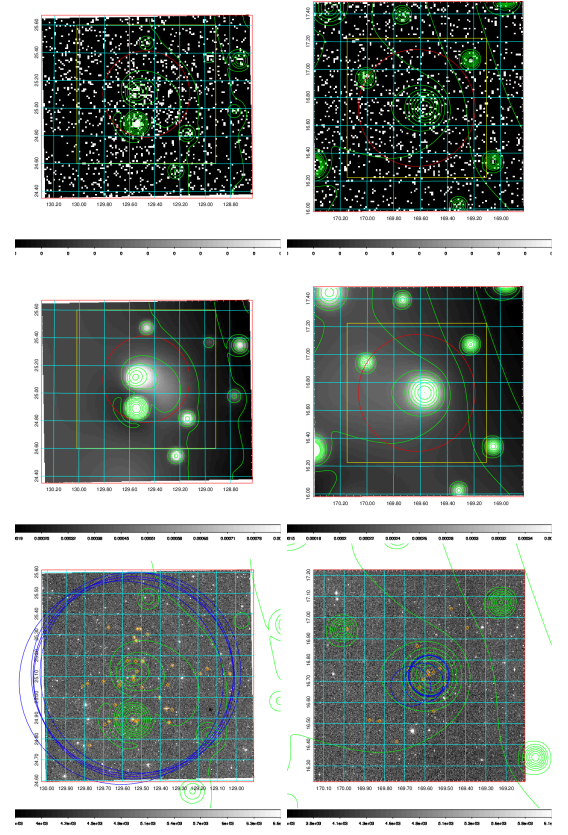


Fig. E.1: Two RXGCC clusters with extent  $> 15'$ . The left column lists images of RXGCC 296 and the right column for RXGCC 400. In every column, the panels show, in the sequence of top to bottom, the RASS image in  $[0.5 - 2.0]$  keV, reconstructed image with wavelet filtering, DES image, SDSS image, and the redshift histogram. In the first two rows, the center and radius of red circles indicate the position and extent of the candidate, while green contours are obtained from the reconstructed image indicating the smoothed X-ray emission. The images in the third and fourth rows are with the size of  $1^\circ \times 1^\circ$ , which is labeled with the yellow box in the first two rows. The DES images are overlaid with yellow diamonds and blue circles for galaxies and galaxy clusters with  $\Delta z < 0.01$ , respectively. The radius of blue circles is 1 Mpc. The red cross in the fourth panel labels the position of our candidate. The redshift distribution of galaxies with the offset  $< 15'$  and  $< 0.5$  Mpc is shown in the last row, which is overlaid with the redshift of previous optical and ICM-detected clusters respectively in red and green histograms. The redshift of the candidate is shown in solid black line, while the upper and lower limits of  $1\sigma$  are shown with black dotted lines.